FERMILAB-PUB-13-386-PPD

Constraining anomalous HVV interactions at proton and lepton colliders

Ian Anderson,[1] Sara Bolognesi,[1] Fabrizio Caola,[1] Yanyan Gao,[2] Andrei V. Gritsan,[1] Christopher B. Martin,[1] Kirill Melnikov,[1] Markus Schulze,[3] Nhan V. Tran,[2] Andrew Whitbeck,[1] and Yaofu Zhou[1]

[1]*Department of Physics and Astronomy, Johns Hopkins University, Baltimore, MD 21218, USA*
[2]*Fermi National Accelerator Laboratory (FNAL), Batavia, IL 60510, USA*
[3]*Argonne National Laboratory (ANL), Lemont, IL 60439, USA*

(Dated: September 19, 2013)

In this paper, we study the extent to which *CP* parity of a Higgs boson, and more generally its anomalous couplings to gauge bosons, can be measured at the LHC and a future electron-positron collider. We consider several processes, including Higgs boson production in gluon and weak boson fusion and production of a Higgs boson in association with an electroweak gauge boson. We consider decays of a Higgs boson including $ZZ, WW, \gamma\gamma$, and $Z\gamma$. Matrix element approach to three production and decay topologies is developed and applied in the analysis. A complete Monte Carlo simulation of the above processes at proton and e^+e^- colliders is performed and verified by comparing it to an analytic calculation. Prospects for measuring various tensor couplings at existing and proposed facilities are compared.

PACS numbers: 12.60.-i, 13.88.+e, 14.80.Bn

I. INTRODUCTION

The existence of a Higgs boson with the mass around 125 GeV has now been firmly established by the ATLAS and CMS experiments at the Large Hadron Collider [1, 2] with supporting evidence from the Tevatron experiments [3]. However, detailed understanding of the properties of this particle will require an array of precision measurements of Higgs boson production and decay processes. The purpose of this paper is to present a coherent framework for studying anomalous couplings of a Higgs boson in processes which involve its interactions with weak vector bosons, photons, and gluons. We develop tools for measuring the anomalous couplings and compare the expected sensitivity in different modes at existing and planned experimental facilities.

Several facts about Higgs boson spin, parity, and its couplings have already been established. The new boson cannot have spin one because it decays to two on-shell photons [4]. The spin-one assignment is also strongly disfavored by the measurement of angular distributions in $H \to ZZ$ decays [5, 6]. Under the assumption of minimal coupling to vector bosons or fermions, the new boson is unlikely to be a spin-two particle [5, 6]. The spin-zero, negative parity hypothesis is also strongly disfavored [5, 6]. Therefore, the new particle appears to be predominantly a $J^{CP} = 0^{++}$ state whose couplings to gauge bosons may, however, have small anomalous components. Constraining and possibly measuring these anomalous couplings will require an extensive experimental program.

The basic idea behind any spin-parity measurement is that different spin-parity assignments restrict the allowed types of interactions between the Higgs boson and other particles. This feature manifests itself in various kinematic distributions of either the decay products of the Higgs particle or particles produced in association with it. There are three processes that can be used to determine the Lorentz structure of the HVV interaction vertex, where V stands for a vector boson Z, W, γ, g, cf. Figs. 1, 2. They are

- production of a Higgs boson (in any process) followed by its decay to two vector bosons followed by a decay to fermions, such as $H \to ZZ, WW \to 4f$, $H \to Z\gamma \to 2f\gamma$, see left panes in Figs. 1, 2, where definition of kinematic observables through the particle momenta can be found in Refs. [7, 8];
- production of $Z^*(W^*)$ followed by its decay into Z or W and a Higgs boson. The Higgs boson then decays into any final state, see middle panes in Figs. 1, 2;
- production of a Higgs boson in association with two jets in weak boson fusion or gluon fusion, followed by the Higgs boson decay into any final state, see right panes in Figs. 1, 2.

Many of these processes were already studied from the point of view of spin-parity determination [7–36]. The goal of this paper is to combine all these studies into a single framework and estimate the ultimate sensitivity to anomalous couplings that can be reached at the LHC and future lepton colliders.

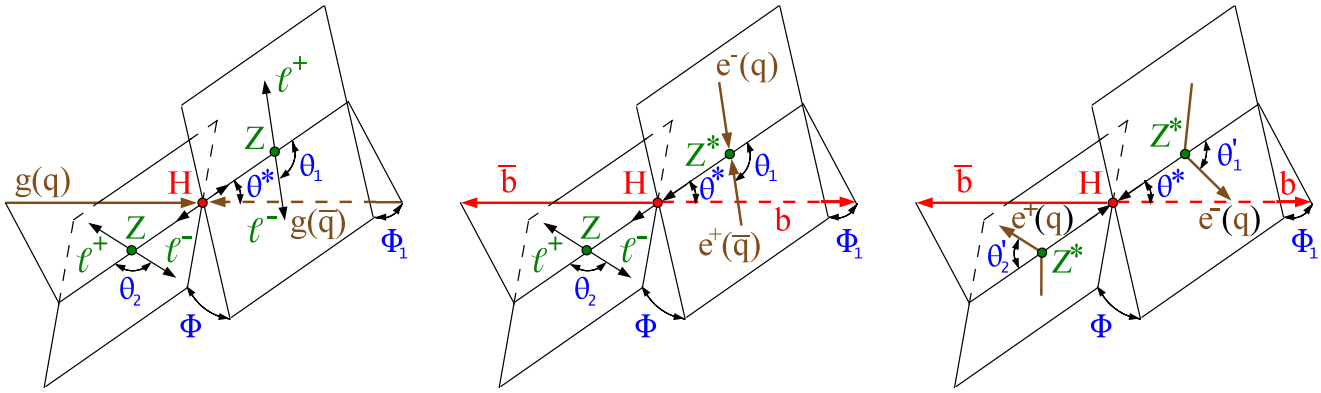

FIG. 1: Illustrations of H particle production and decay in pp or e^+e^- collision $gg/q\bar{q} \to H \to ZZ \to 4\ell^\pm$ (left), $e^+e^-(q\bar{q}) \to Z^* \to ZH \to \ell^+\ell^- b\bar{b}$ (middle), or $e^+e^-(qq') \to e^+e^-(qq')H \to e^+e^-(qq')b\bar{b}$ (right). The $H \to b\bar{b}$ decay and HZZ coupling are shown as examples, so that Z can be substituted by other vector bosons. Five angles fully characterize the orientation of the production and decay chain and are defined in the suitable rest frames.

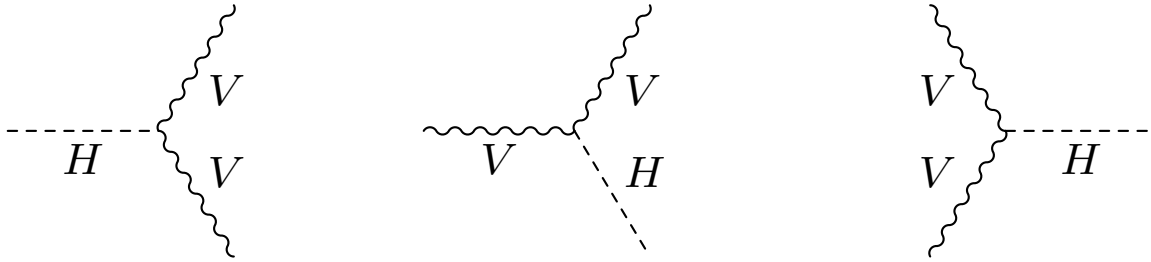

FIG. 2: Illustration of an effective HVV coupling, where $V = Z, W, \gamma, g$ with H decay to two vector bosons (left), associated H production with a vector boson (middle), and vector boson fusion (right).

We build upon our previous analysis of this problem described in Refs. [7, 8]. Techniques developed there are well-suited for measuring HVV anomalous couplings since these couplings affect angular and mass distributions and can be constrained by fitting observed distributions to theory predictions. However, such multi-parameter fits require large samples of signal events that are currently not available. Nevertheless, it is interesting to study the ultimate precision on anomalous couplings that can be achieved at the LHC and a future lepton collider since the expected number of events can be easily estimated.

We organize the rest of the paper as follows. In Section II we briefly review parameterization of the HVV vertex. In Section III we discuss Monte Carlo and likelihood techniques, since they provide the necessary tools for the experimental studies. In Section IV we explore various approaches to anomalous couplings measurements and summarize the precision that is achievable at different facilities. We conclude in Section V. Additional details, including discussion of the matrix element method and methodology of the analysis, can be found in Appendices.

II. PARAMETRIZATION OF THE SCATTERING AMPLITUDES

Studies of spin, parity, and couplings of a Higgs boson employ generic parameterizations of scattering amplitudes. Such parameterizations contain all possible tensor structures consistent with assumed symmetries and Lorentz invariance. We follow the notation of Refs. [7, 8] and write the general scattering amplitude that describes interactions of a spin-zero boson with the gauge bosons, such as ZZ, WW, $Z\gamma$, $\gamma\gamma$, or gg

$$A(X_{J=0} \to VV) = v^{-1}\left(g_1 m_V^2 \epsilon_1^* \epsilon_2^* + g_2 f_{\mu\nu}^{*(1)} f^{*(2),\mu\nu} + g_3 f^{*(1),\mu\nu} f_{\mu\alpha}^{*(2)} \frac{q_\nu q^\alpha}{\Lambda^2} + g_4 f_{\mu\nu}^{*(1)} \tilde{f}^{*(2),\mu\nu}\right) . \quad (1)$$

In Eq. (1), $f^{(i),\mu\nu} = \epsilon_i^\mu q_i^\nu - \epsilon_i^\nu q_i^\mu$ is the field strength tensor of a gauge boson with momentum q_i and polarization vector ϵ_i; $\tilde{f}^{(i),\mu\nu} = 1/2\epsilon^{\mu\nu\alpha\beta} f_{\alpha\beta}$ is the conjugate field strength tensor. Parity-conserving interactions of a scalar (pseudoscalar) are parameterized by the couplings $g_{1,2,3}(g_4)$, respectively. In the Standard Model (SM), the only non-vanishing coupling of the Higgs to ZZ or WW bosons at tree-level is $g_1 = 2i$, while g_2 is generated through radiative corrections.

For final states with at least one massless gauge boson, such as $\gamma\gamma$, gg or $Z\gamma$, the SM interactions with the Higgs boson are loop-induced; these interactions are described by the coupling g_2. The coupling g_3 can be absorbed into the g_2 if the coupling constants are treated as momentum-dependent form factors [7, 8]. Moreover, this term is supposed to be small since it corresponds to a dimension-seven operator in an Effective Lagrangian framework. We therefore neglect the g_3 term in the following discussion, but we note that it can be easily included if necessary.

In this paper, we focus on the determination of anomalous couplings of the $J^{CP} = 0^{++}$ Higgs-like boson to SM gauge bosons since existing experimental data already disfavors other exotic spin-parity assignments [5, 6]. For HZZ or HWW vertices, we therefore assume that the coupling constants satisfy a hierarchical relation $g_1 \gg g_{2,4}$ and that non-standard couplings *always* provide small modifications of the SM contributions.

It is convenient to express the results of the measurement of the anomalous couplings in terms of physical quantities. To this end, we consider three independent complex couplings g_1, g_2, and g_4 for each coupling to vector bosons Z, γ, W, g. Five independent numbers are needed to parameterize the couplings since one overall complex phase is not measurable. We take one of these numbers to be the $H \to VV$ decay rate; the remaining four real numbers parameterize ratios of couplings and their relative phases. We find it convenient to use effective fractions of events defined as

$$f_{gi} = \frac{|g_i|^2\sigma_i}{|g_1|^2\sigma_1 + |g_2|^2\sigma_2 + |g_4|^2\sigma_4}, \tag{2}$$

to parameterize couplings ratios. The phases are defined as $\phi_{gi} = \arg(g_i/g_1)$. We note that σ_i in Eq. (2) is the cross-section for the process $H \to VV$, $V^* \to VH$, or $V^*V^* \to H$ that corresponds to $g_i = 1, g_{j\neq i} = 0$. The advantage of introducing fractions f_{gi} is that, for fixed tensorial structure of the HVV vertex, they are invariant under independent re-scalings of all couplings. They may also be interpreted as fractions of event yields corresponding to each anomalous coupling independently. Contributions that originate from interferences of different amplitudes can be described using parameterization introduced above; for this, both fractions f_{gi} and phases ϕ_{gi} are required. Once fractions f_{gi} are measured, one can extract the coupling constants in a straightforward way by inverting Eq. (2), e.g. $|g_i/g_1| = (f_{gi}/(1-\sum_k f_{gk}))^{1/2} \times (\sigma_1/\sigma_i)^{1/2}$. The parameter f_{g4} is equivalent to the parameter f_{a3} as introduced by the CMS collaboration [5] under the assumption $g_2 = 0$; it is the fraction of a *CP*-odd contribution to the total production cross section of a Higgs boson. For the ease of comparison with earlier CMS studies, we will use f_{a2} and f_{a3} instead of f_{g2} and f_{g4}, respectively, to denote event fractions throughout the paper. The $f_{a2}^{\rm dec}$ and $f_{a3}^{\rm dec}$ values correspond to cross-sections defined in decay $H \to VV$.

III. ANALYSIS TOOLS

Analyses reported in this paper require a simulation program to describe production of resonances in hadron-hadron or e^+e^- collisions, followed by their subsequent decays. Anomalous couplings to vector bosons must be included. The simulation program is supplemented by both analytical and numerical calculations of the likelihood distributions based on the matrix element method. These analysis tools are described in this Section. Additional details can be found in Appendices.

Events are simulated with the JHU generator [7, 8, 37], a dedicated Monte Carlo program, that features implementations of the processes $gg/q\bar{q} \to X \to ZZ(WW) \to 4f$ as well as $gg/q\bar{q} \to X \to \gamma\gamma$. The JHU generator incorporates all spin correlations, interference of all contributing amplitudes, and the general couplings of the X particle to gluons and quarks in production and to vector bosons in decay. New features of the JHU generator, implemented since the last release, are summarized below.

The JHU generator has been extended to include new processes: associated production of a Higgs boson in either proton or electron collisions $q\bar{q}' \to V^* \to VH$, $e^+e^- \to Z^* \to ZH$, and associated production with two jets from either gluon fusion $gg \to H + 2$ jets or weak boson fusion $qq' \to qq'V^*V^* \to Hqq'$, where $V = Z, W$. In all cases, parameterization of the HVV vertex with all anomalous couplings as in Eq. (1) is included. We also introduce the decay mode $H \to Z\gamma$. Extension to other spin assignments of an exotic boson following formalism in Refs. [7, 8] is also available for some of these processes, but it is not the focus of the study presented here.

Another feature of the generator implemented recently concerns the dependence of the effective coupling constants $g_{1\ldots4}$ on the virtualities of two vector bosons, cf. Eq. (1). To describe this effect, we parameterize the couplings as

$$g_i(q_1^2, q_2^2) = g_i^{\rm SM} + g_i' \times \frac{\Lambda_i^4}{(\Lambda_i^2 + |q_1^2|)\,(\Lambda_i^2 + |q_2^2|))}\,, \tag{3}$$

where Λ_i is the energy scale that is correlated with masses of new, yet unobserved, particles that contribute to HVV interaction vertex and $g_i^{\rm SM} = g_1 \cdot \delta_{i1}$ appears at tree level in the coupling of a Higgs boson to weak vector bosons in

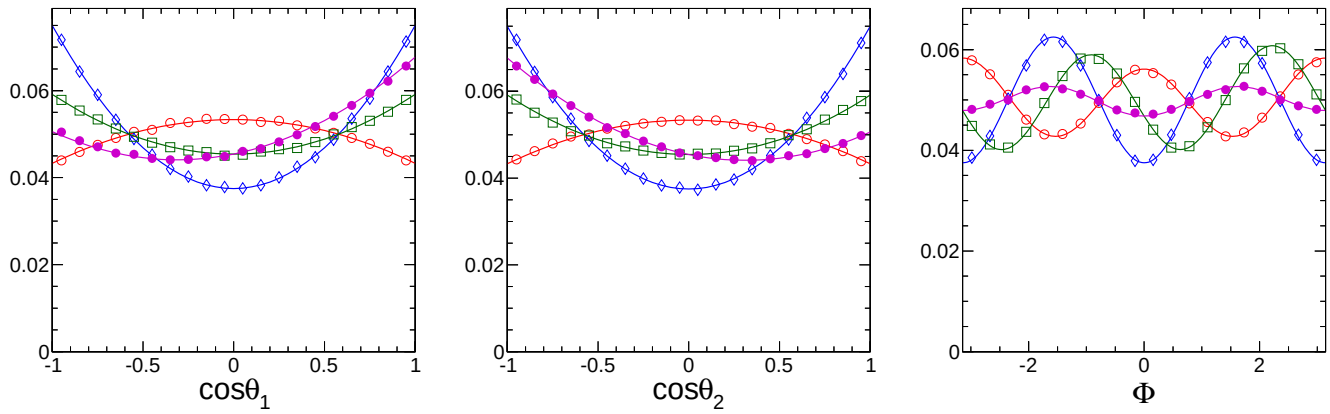

FIG. 3: Distributions of the observables in the $e^+e^- \to ZH \to (\ell^+\ell^-)H$ analysis at $\sqrt{s} = 250$ GeV, from left to right: $\cos\theta_1$, $\cos\theta_2$, and Φ. Points show simulated events and lines show projections of analytical distributions. Four scenarios are shown: SM scalar (0^+, red open circles), pseudoscalar (0^-, blue diamonds), and two mixed states corresponding to $f_{a3} = 0.5$ with $\phi_{a3} = 0$ (green squares) and $\pi/2$ (magenta points). In all cases we choose $f_{a2} = 0$.

the Standard Model. Although we do not use this feature of the generator in the current paper, we expect that it will be helpful for checking the sensitivity of various observables employed for spin-parity analysis to high-energy or high invariant-mass tails of kinematic distributions that may be affected by poorly controlled form-factor effects.

The generator program can be interfaced to parton shower simulation as well as full detector simulation through the Les Houches Event (LHE) file format [38]. The JHU generator now also allows interfacing the decay of a spin-zero particle with the production simulated by other MC programs, or by the JHU generator itself, through the LHE file format. This option allows us to combine modeling of the NLO QCD effects in the production of a 0^+ particle with the description of its decays that includes both anomalous couplings and interference effects of identical fermions in the final state.

Apart from simulating events, our analysis requires the construction of various likelihood functions to distinguish between different hypotheses about the Lorentz structure of the HVV interaction vertex. As described in Appendix A, the likelihood functions are obtained from kinematic probability distributions that can be either computed analytically or numerically. Analytical parameterizations are currently available for the $H \to VV$, $pp \to VH$, and $e^+e^- \to ZH$ processes, see Appendix A and Refs. [7, 8]. Numerical computations of matrix elements are provided by the JHU generator. These matrix elements are also needed to compute cross-sections and kinematics distributions. The matrix elements are implemented in the JHU generator as separate functions [8] and can be accessed by an end-user directly. We provide the necessary codes to compute the likelihood functions using both analytic and numerical parameterizations of the matrix elements [37].

The availability of the two methods allows independent validation of the same analysis. Results presented in this paper employ analytic parameterization of the probabilities when available. This allows analytic normalization of the probability distributions to facilitate multi-dimensional and multi-parameter fits. When analytic results are not available, we use numerical computations of the matrix element squared.

Examples of both analytical and generator distributions are shown in Fig. 3 for the $e^+e^- \to ZH \to (\ell^+\ell^-)H$ process. More examples are available in Refs. [7, 8] for decay processes and in Appendix A for the production and decay processes at the LHC. Examples of analyses based on the implementation of the matrix element techniques are given in Appendix B. We will use the distributions in Fig. 3 to explain some results obtained in the next Section.

IV. MEASUREMENTS OF HVV ANOMALOUS COUPLINGS

In this Section we describe prospects for measuring the anomalous HVV couplings both at the LHC and at a future e^+e^- collider. We consider all types of processes that allow such measurements, including weak boson fusion, gluon fusion (LHC), and VH production. For the analysis of the Higgs boson decay $H \to VV$, all production mechanisms can be combined. The cleanest and most significant SM Higgs decay mode at the LHC is $H \to ZZ^* \to 4\ell$ and we consider this mode in the following analysis [5, 6]. Inclusion of other decay modes will only improve estimated precision and we examine such examples as well ($H \to \gamma\gamma$ in VBF and $H \to b\bar{b}$ in VH production). At an e^+e^- collider, we consider the dominant decay mode $H \to b\bar{b}$, but other final states could be considered as well.

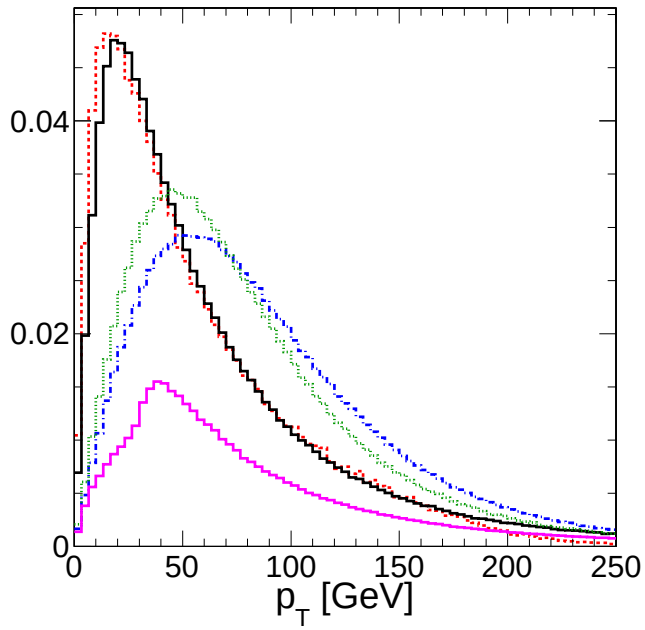

FIG. 4: Comparison of transverse momentum p_T distribution of a SM Higgs boson with $m_H = 125$ GeV in MC simulation of 14 TeV pp collisions at LHC. Production in gluon fusion is generated by the JHU generator combined with Pythia parton shower (dashed red) and NLO QCD matched to parton shower in POWHEG (solid black), with decay $H \to ZZ \to 4\ell$ simulated using the JHU generator in both cases. Also shown are VH production (dotted green), weak VBF production (dot-dashed blue), and gluon fusion $H + 2$ jets production (solid magenta) with the JHU generator. All distributions are normalized to unit area except for $H + 2$ jets, which is normalized to the relative fraction with respect to inclusive gluon fusion production according to cross section with selection requirements on jets $p_T > 15$ GeV and $\Delta R_{jj} > 0.5$ as discussed in text.

We now discuss details of event simulation and selection. In this paper, signal events were simulated with the JHU generator. Background events were generated with POWHEG [39] ($q\bar{q} \to ZZ^{(*)}/Z\gamma^{(*)}$ + jets) and MadGraph [40] ($q\bar{q} \to ZZ^{(*)}/Z\gamma^{(*)}/\gamma\gamma$ + 0 or 2 jets, $e^+e^- \to ZZ$). When backgrounds from other processes are expected, their effective contribution is included by rescaling the expected event yields of the aforementioned processes. The VBF and VH topology of the SM Higgs boson production has been tested against VBF@NLO [41–43] and MadGraph simulation, respectively.

To properly simulate recoil of the final state particles caused by QCD radiation, the JHU generator can be interfaced with Pythia [44], or alternatively to POWHEG for spin-zero particle production. We note that quality of the approximation with Pythia parton showering is surprisingly high as can be seen in Fig. 4 where we compare the transverse momentum distribution of a Standard Model Higgs boson obtained within this framework with the NLO QCD computation of the same distribution as implemented in POWHEG. Effects of BSM couplings in production on recoil of the final state particles caused by the QCD radiation have been tested explicitly in the $pp \to H + 2$ jets process; we found that their impact on recoil kinematics is negligible for the analysis of Higgs decays. We conclude that parton shower description of QCD effects is sufficient at the current level of analysis but further refinements of such an approach, for example by means of dedicated NLO QCD computations, are certainly possible, see e.g. Ref. [32].

In this paper, we employ a simplified detector simulation similar to our earlier studies [7, 8]. Lepton momenta are smeared with an rms $\Delta p/p = 0.014$ for 90% of events and a broader smearing for the remaining 10%. Hadronic jets are smeared with an rms $\Delta p/p = 0.1$. Events are selected in which leptons have $|\eta| < 2.4$, and transverse momentum $p_T > 5\,\text{GeV}$; jets, defined with anti-$k_\perp$ algorithm, have $\Delta R_{jj} > 0.5$, $p_T > 30\,\text{GeV}$, and $|\eta_j| < 4.7$. The jet p_T threshold is raised to 50 GeV to study the effects of pileup when we consider the high luminosity LHC scenario. The invariant mass of the di-lepton pairs from a $Z^{(*)}$ decay is required to exceed 12 GeV. These selection criteria are chosen to be as close as possible to existing LHC analyses [5, 6] and we assume that similar selection criteria will be also adopted for a future e^+e^- collider. The estimated number of reconstructed events in Table I is scaled down from the number of produced events by 30% and 80% at pp and e^+e^- colliders, respectively. The ZH channel with $H \to b\bar{b}$ accounts for tighter selection requirements discussed in text.

The expected statistical precision of the analysis depends on the number of Higgs bosons produced at each collider which is proportional to collider's integrated luminosity. To estimate the number of Higgs bosons expected at the

TABLE I: Summary of collider options considered for the production of a Higgs boson with the mass of 125 GeV. Collider center-of-mass energy, integrated luminosity, cross-sections for relevant production modes and decay channels are shown. Reconstructed efficiencies are estimated using selection criteria described in the text and relate the number of produced and reconstructed events ($N_{\rm prod}$ and $N_{\rm reco}$). In several cases we also show fractions $f_{\rm jet}$ of events with two associated jets with $p_T > 30$ GeV and $\Delta R_{jj} > 0.5$.

collider	energy	$\int \mathcal{L}dt$ (fb^{-1})	production	σ (fb)	decay	$\sigma \times \mathcal{B}$ (fb)	$N_{\rm prod}$	$N_{\rm reco}$	$f_{\rm jet}$
pp	14 TeV	3000	$gg \to H$	49850	$H \to ZZ^* \to 4\ell$	6.23	18694	5608	0.1
pp	14 TeV	3000	$V^*V^* \to H$	4180	$H \to ZZ^* \to 4\ell$	0.52	1568	470	0.6
pp	14 TeV	3000	$W^* \to WH$	1504	$H \to ZZ^* \to 4\ell$	0.19	564	169	0.5
pp	14 TeV	3000	$Z^* \to ZH$	883	$H \to ZZ^* \to 4\ell$	0.11	331	99	0.5
pp	14 TeV	3000	$t\bar{t} \to t\bar{t}H$	611	$H \to ZZ^* \to 4\ell$	0.08	229	69	1.0
pp	14 TeV	3000	$V^*V^* \to H$	4180	$H \to \gamma\gamma$	9.53	28591	8577	0.6
pp	14 TeV	3000	$Z^* \to ZH$	883	$H \to b\bar{b}$, $Z \to \ell\ell$	34.3	102891	690	–
e^+e^-	250 GeV	250	$Z^* \to ZH$	240	$H \to b\bar{b}$, $Z \to \ell\ell$	9.35	2337	1870	–
e^+e^-	350 GeV	350	$Z^* \to ZH$	129	$H \to b\bar{b}$, $Z \to \ell\ell$	5.03	1760	1408	–
e^+e^-	500 GeV	500	$Z^* \to ZH$	57	$H \to b\bar{b}$, $Z \to \ell\ell$	2.22	1110	888	–
e^+e^-	1 TeV	1000	$Z^* \to ZH$	13	$H \to b\bar{b}$, $Z \to \ell\ell$	0.51	505	404	–
e^+e^-	250 GeV	250	$Z^*Z^* \to H$	0.7	$H \to b\bar{b}$	0.4	108	86	–
e^+e^-	350 GeV	350	$Z^*Z^* \to H$	3	$H \to b\bar{b}$	1.7	587	470	–
e^+e^-	500 GeV	500	$Z^*Z^* \to H$	7	$H \to b\bar{b}$	4.1	2059	1647	–
e^+e^-	1 TeV	1000	$Z^*Z^* \to H$	21	$H \to b\bar{b}$	12.2	12244	9795	–

LHC and at a future e^+e^- collider we note that each of the two LHC experiments will collect 300 fb^{-1} of integrated luminosity at pp collision energy of about 14 TeV. Beyond that, a high-luminosity upgrade is planned where 3000 fb^{-1} per experiment are expected to be collected [45, 46]. Among future facilities, an e^+e^- collider operating at the center-of-mass energies of 250 GeV and above with either linear [47] or circular [48] design could deliver a luminosity that ranges from several hundred to several thousand fb^{-1}. At an e^+e^- collider the ZH production dominates at lower energies while at higher energies WW or ZZ fusion dominates. However, although $e^+e^- \to \nu\bar{\nu}W^*W^* \to \nu\bar{\nu}H$ cross section exceeds the cross section for $e^+e^- \to e^+e^-Z^*Z^* \to e^+e^-H$ by about an order of magnitude, no angular analysis is possible in final states with neutrinos.

The resulting numbers of a 125 GeV Standard Model (SM) Higgs bosons expected at the LHC and at an e^+e^- collider are summarized in Table I. We calculalte the number of produced signal events $N_{\rm prod}$ using SM Higgs boson cross-sections and branching fractions from Ref. [10]. The cross-sections at an e^+e^- collider are calculated with the JHU generator for $e^+e^- \to ZH$ process and MadGraph for $e^+e^- \to e^+e^-H$ VBF-only process. The selection criteria described above are used to find the number of reconstructed Higgs bosons $N_{\rm reco}$. We assume only small contributions of anomalous couplings which would not change this number significantly. The LHC experiments are expected to collect sufficient statistics to study HVV tensor structure both in production and in decay of a Higgs boson. At the same time, the e^+e^- machines are in a much better position to study the HVV tensor structure in production, especially at high energy. However, considerations based entirely on event yields are insufficient since both kinematics and relative importance of various tensor structures' contributions change depending on the process and collision energies. To illustrate this, in Table II we show examples where cross-sections σ_i, defined below Eq. (2), are computed for several processes.

As evident from Table II, relative cross-sections corresponding to scalar (g_1) and pseudoscalar (g_4) couplings are different in various HVV processes. For example the ratio σ_4/σ_1 is 0.153 in the $H \to ZZ$ decay, 8.07 in $e^+e^- \to ZH$ production at $\sqrt{s} = 250$ GeV and grows linearly with increasing $\sqrt{s}$. This is caused by the different dependence of the scalar and pseudoscalar tensor couplings in Eq. (1) on the off-shellness of the vector boson, which leads to an asymptomatically energy-independent e^+e^- cross-section in case of CP-odd higher-dimensional operator. This feature means that, for a fixed ratio of coupling constants $|g_4/g_1|$, it is beneficial to go to highest available energy where the production cross-section due to g_4 is kinematically enhanced [28]. Therefore, the same fraction of events for CP-odd contributions at different collider energies translates into different sensitivities for effective couplings g_i. To compare different cases, we express the results of the analysis in terms of $f_{a3}^{\rm dec}$, defined for the Higgs decay to two vector bosons since in this case the kinematics are entirely fixed and this choice determines the ratio of the coupling constants uniquely.

TABLE II: Description of processes used for HVV tensor structure measurements with the corresponding cross-sections ratios, where σ_1, σ_2, or σ_4 corresponds to $g_1 = 1$, $g_2 = 1$, or $g_4 = 1$, respectively, and $\sigma_+ = \sigma_1$ ($g_+ = g_1$) for all processes except couplings to massless vector bosons ($Z\gamma, \gamma\gamma, gg$) where $\sigma_+ = \sigma_2$ ($g_+ = g_2$). MC simulation parameters used in studies are shown, where the generated coupling g_i values correspond to certain f_{a2} and f_{a3} values. The expected precision on the f_{a2} and f_{a3} parameters are quoted for 300 fb^{-1} (first row) and 3000 fb^{-1} (second row) scenarios on LHC and four energy scenarios on an e^+e^- machine, as discussed in Table I. This expected precision corresponds to about 3σ deviation from zero of the MC simulated values. The $f_{a2}^{\rm dec}$ and $f_{a3}^{\rm dec}$ values correspond to cross-sections defined in decay.

process description					MC simulation parameters						expected precision			
collider	energy	mode	σ_2/σ_1	σ_4/σ_+	$\lvert g_2/g_1\rvert$	$\lvert g_4/g_+\rvert$	f_{a2}	$f_{a2}^{\rm dec}$	f_{a3}	$f_{a3}^{\rm dec}$	δf_{a2}	$\delta f_{a2}^{\rm dec}$	δf_{a3}	$\delta f_{a3}^{\rm dec}$
any	any	$H \to ZZ^*$	0.362	0.153	0	1.20	0		0.18		–		0.06	
					0	0.67	0		0.06		–		0.02	
					0.78	0	0.18		0		0.088		–	
					0.42	0	0.06		0		0.014		–	
any	any	$H \to WW^*$	0.776	0.322	0	1.76	0		0.50		–		–	
					1.13	0	0.50		0		–		–	
any	any	$H \to \gamma\gamma, gg$	N/A	1.0	N/A	1.0	0		0.50		–		–	
any	any	$H \to Z\gamma$	N/A	1.0	N/A	1.0	0		0.50		–		–	
pp	14 TeV	$gg \to H$	N/A	1.0	N/A	1.0	0	0	0.50	0.50	–		0.50	0.50
		$(H \to ZZ^*)$			N/A	1.0	0	0	0.50	0.50	–		0.16	0.16
pp	14 TeV	$V^*V^* \to H$	14.0	11.3	0	0.299	0	0	0.50	0.013	–		0.190	7×10^{-3}
		$(H \to ZZ^*)$			0	0.109	0	0	0.12	0.0018	–		0.036	6×10^{-4}
pp	14 TeV	$V^*V^* \to H$	14.0	11.3	0	0.109	0	0	0.12	0.0018	–		0.04	7×10^{-4}
		$(H \to \gamma\gamma)$			0	0.052	0	0	0.030	0.0004	–		0.009	1.3×10^{-4}
pp	14 TeV	$V^* \to VH$	76.1	46.8	0	0.145	0	0	0.50	0.0032	–		0.32	3×10^{-3}
		$(V \to q\bar{q}', H \to ZZ^*)$			0	0.095	0	0	0.30	0.0014	–		0.10	6×10^{-4}
pp	14 TeV	$V^* \to VH$	76.1	46.8	0	0.061	0	0	0.15	0.0006	–		0.09	4×10^{-4}
		$(V \to \ell^+\ell^-, H \to b\bar{b})$			0	0.049	0	0	0.10	0.0004	–		0.029	1.2×10^{-4}
e^+e^-	250 GeV	$Z^* \to ZH$	34.1	8.07	0	0.117	0	0	0.10	2×10^{-3}	–		0.032	7×10^{-4}
					0.057	0	0.10	1.2×10^{-3}	0	0	0.033	4×10^{-4}		–
e^+e^-	350 GeV	$Z^* \to ZH$	84.2	50.6	0	0.0469	0	0	0.10	3×10^{-4}	–		0.031	1.1×10^{-4}
					0.025	0	0.05	2×10^{-4}	0	0	0.015	7×10^{-5}		–
e^+e^-	500 GeV	$Z^* \to ZH$	200.8	161.1	0	0.0263	0	0	0.10	1.1×10^{-4}	–		0.034	4×10^{-5}
					0.024	0	0.10	2×10^{-4}	0	0	0.033	7×10^{-5}		–
e^+e^-	1 TeV	$Z^* \to ZH$	916.5	870.8	0	0.0113	0	0	0.10	2×10^{-5}	–		0.037	8×10^{-6}
					0.014	0	0.15	7×10^{-5}	0	0	0.049	3×10^{-5}		–

To illustrate this point further, we examine the energy dependence of the $e^+e^- \to Z^* \to ZH$ cross section for various tensor couplings. In Fig. 5, cross section dependence on $\sqrt{s}$ is shown for the ratio of the coupling constants chosen in such a way that cross sections for all tensor structures at $\sqrt{s} = 250$ GeV are equal to the SM $e^+e^- \to Z^* \to ZH$ cross-section. The threshold behavior for $\sqrt{s} < 250$ GeV of the cross-sections $e^+e^- \to Z^* \to XZ$ has been suggested as a useful observable to determine the spin of the new boson [14]. Similarly, in a mixed CP-case, the dependence of $e^+e^- \to ZH$ cross-section on the energy of the collision will differ from a pure $J^{CP} = 0^{++}$ case; therefore, a measurement of the cross-section at several different energies will give us useful information about anomalous HVV couplings. For example, if the $e^+e^- \to Z^* \to ZH$ cross-section is first measured at the center of mass energy $\sqrt{s} = 250$ GeV, the scan of cross-sections at 350, 500, and 1000 GeV will lead to a measurement of $f_{a3} = 0.035, 0.041$, and 0.055, respectively, using the expected signal yields reported in Table I. This would translate to precision on $f_{a3}^{\rm dec}$ of $10^{-4}, 4\times10^{-5}$, and 10^{-5}, respectively, as defined in the decay $H \to ZZ^*$.

As we have already mentioned, the reason for the significantly improved precision on f_{a3} that appears to be achievable at higher energy e^+e^- colliders is the energy-independence of the cross section for pseudoscalar couplings, caused by the non-renormalizable nature of the operator $Z_{\mu\nu}\tilde{Z}^{\mu\nu}$. Of course, this feature cannot continue forever and, in any theory, the coupling "constant" g_4 should eventually become a q^2-dependent form factor, which will

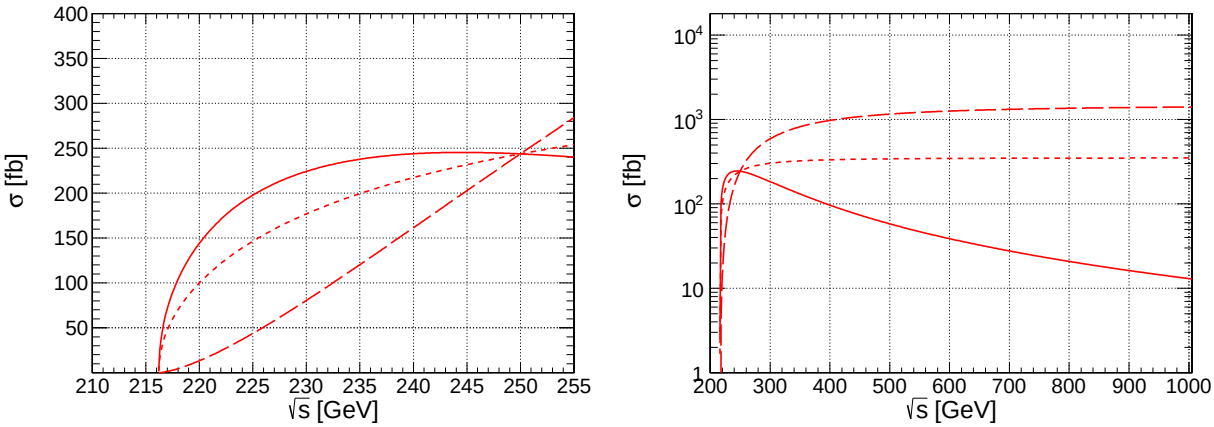

FIG. 5: Cross-sections for $e^+e^- \to Z^* \to ZX$ process as a function of $\sqrt{s}$ for three models: SM Higgs (0^+, solid), scalar with higher-dimension operators (0^+_h, short-dashed), and pseudoscalar (0^-, long-dashed). All cross-sections are normalized to SM value at $\sqrt{s} = 250$ GeV. Different high-energy behavior of cross-sections related to point-like interactions (solid) and higher-dimensional non-renormalizable operators (dashed) is apparent from the right pane.

provide suppression for the cross-section at higher energies. The energy scale where the q^2-dependence of the effective couplings can no longer be ignored is denoted as Λ_4 in Eq. (3) and we do not know this scale a priori. For this reason, we ignore the q^2-dependent form-factors in this paper, but we note that results presented above can be changed to incorporate possible reduction of the coupling constants with energy.

We conclude this general discussion by pointing out that three types of observables can be used to measure tensor couplings of the Higgs bosons in general and f_{a3} in particular. They are

1. cross-sections, especially their dependences on virtualities of weak bosons [27, 28, 30]. Examples are shown in Fig. 5 for the $e^+e^- \to Z^* \to ZH$ process and in Fig. 13 for the decay $H \to ZZ^*$. We note that while measurements of cross sections in different kinematic regimes appear to be a powerful tool to study anomalous couplings, it relies on our understanding of *dynamics*, rather than kinematics, and therefore may be sensitive to poorly understood form-factor effects or breakdown of effective field-theoretic description.

2. Angular distributions particular to scalar and pseudoscalar HVV interactions or, more generally, to different types of tensor couplings. Examples of such distributions are shown in Figs. 3, 13, 17, 18.

3. Angular distributions or other observables particular to interferences between *CP*-even and *CP*-odd couplings. Examples include forward-backward asymmetry with respect to $\cos\theta_1$ or $\cos\theta_2$ and non-trivial phase in the Φ distributions shown in Figs. 3 and 13. Such asymmetries require undefined *CP* to appear; as the result, *CP* violation would follow as an unambiguous interpretation e.g. once the forward-backward asymmetry is observed.

In order to measure or set a limit on f_{a3}, it is important to employ all types of observables described above and not limit oneself to *CP*-specific ones, such as interferences. In particular, if only a limit is set on f_{a3}, the phase of *CP*-odd contribution ϕ_{a3} is generally unknown and one cannot predict the forward-backward asymmetry in $\cos\theta_1$ nor the non-trivial phase in Φ, as shown in Figs. 3 and 13. In principle, model-dependent assumptions can be made about such phases and tighter constraints on f_{a3} can be obtained, but it is important to pursue coupling measurements that are as model-independent as possible. On the other hand, once a non-zero value of f_{a3} is observed, its phase ϕ_{a3} can be measured directly from the data, as we illustrate below. While we focus on the measurement of the *CP*-odd contribution f_{a3}, we also illustrate measurements of f_{a2}, which can be performed with a similar precision.

A. The $e^+e^- \to ZH$ process

To illustrate the above points, we considered $e^+e^- \to ZH$ process, with $Z \to \ell^+\ell^-$ and $H \to b\bar{b}$. The number of signal events is estimated in Table I for four energies $\sqrt{s} = 250$, 350, 500, 1000 GeV, that are under discussion for an electron-positron collider, and are rounded to 2000, 1500, 1000, 500 events, respectively. The effective number of background events is estimated to be 10% of the number of signal events and is modeled with the $e^+e^- \to ZZ \to \ell^+\ell^- b\bar{b}$ process. Cross-sections for several simulated signal samples are displayed in Table II. We assume that the signal can be reconstructed inclusively by tagging $Z \to \ell^+\ell^-$ decay and using energy-momentum constraints, but

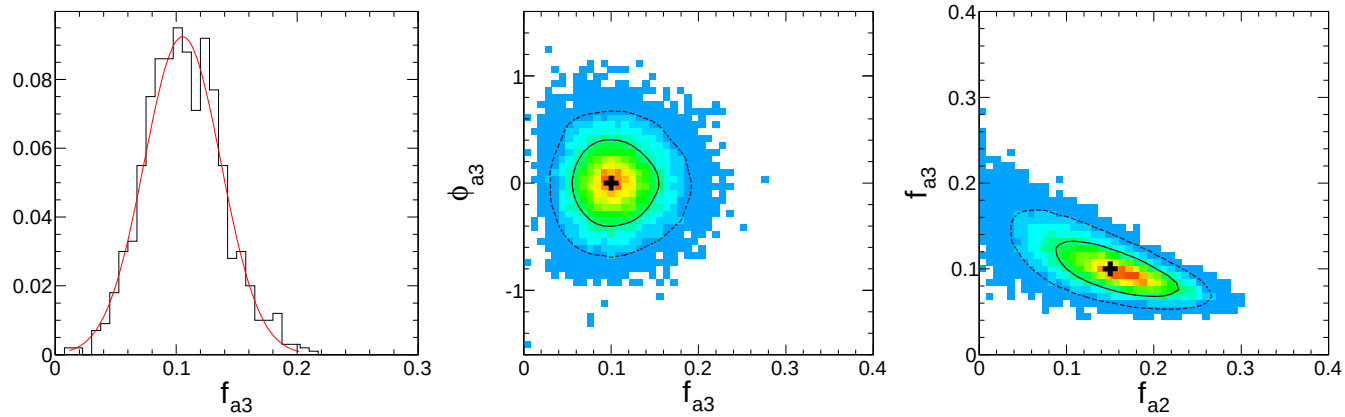

FIG. 6: Distribution of fitted values of f_{a3}, ϕ_{a3}, and f_{a2} in a large number of generated experiments in $e^+e^- \to ZH$ process at $\sqrt{s} = 250$ GeV. Left plot: f_{a3} results from simultaneous fit of f_{a3} and ϕ_{a3}. Middle and right plots: simultaneous fit of f_{a3} and ϕ_{a3} or f_{a3} and f_{a2}, with 68% and 95% confidence level contours shown.

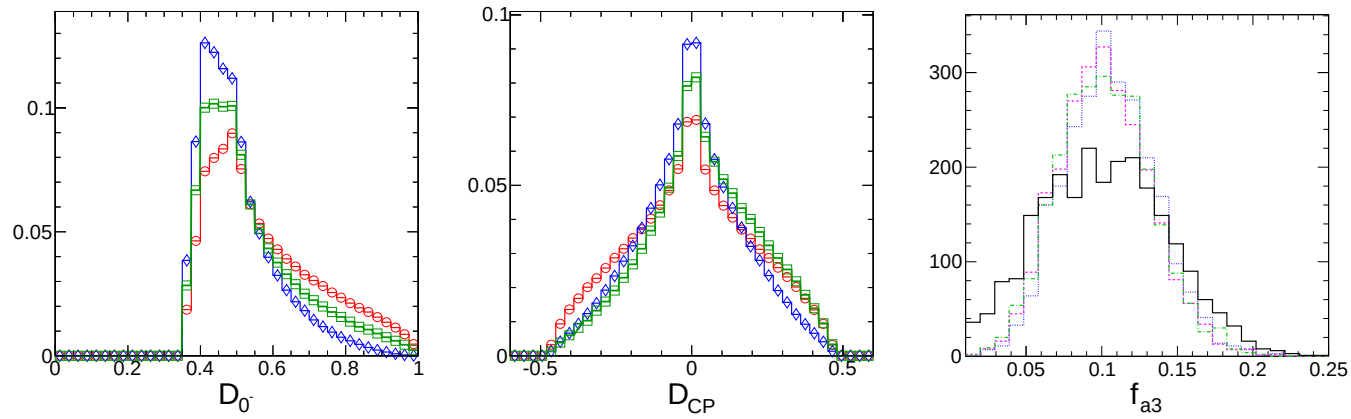

FIG. 7: Distribution of D_{0^-} and D_{CP} for generated events $e^+e^- \to ZH$ at $\sqrt{s} = 250$ GeV. Three processes are shown: SM (0^+, red open circles), pseudoscalar (0^-, blue diamonds), and a mixed state corresponding to $f_{a3} = 0.5$ with $\phi_{a3} = 0$ (green squares). Right plot: f_{a3} results without considering background and detector effects: 1D fit of D_{0^-} (solid black); 2D fit of D_{0^-} and D_{CP} (dot-dashed green); 3D fit with f_{a3} and ϕ_{a3} unconstrained (dotted blue); and 3D fit with f_{a3} only unconstrained (dashed magenta).

further improvements can be achieved through the analysis of the Higgs boson decay products and by considering other Z decay final states. In view of this, our estimates of expected sensitivities are conservative.

Our analysis techniques are identical to what has been used earlier to study Higgs spin and parity in the $pp \to H \to ZZ$ process at the LHC [7, 8]. For this channel and the channels in the following sub-sections, the details of the analyses are explained in Appendix B. We employ either the dedicated discriminants D_{0^-} and D_{CP}, or the multi-dimensional probability distribution. Several thousand statistically-independent experiments are generated and fitted using different approaches. Detector effects and backgrounds are included either with direct parameterization of one- or two-dimensional distributions or by exploiting certain approximations of a multidimensional model, as explained in Appendix B.

For the e^+e^- case discussed in this Section, we first obtained results for the sensitivity to the fractions $f_{a2,a3}$ at fixed collider energy and then expressed these constraints in terms of the parameters $f^{\rm dec}_{a2,a3}$. Figure 6 shows precision on f_{a3} and f_{a2} obtained with generated experiments that include background. Expected precisions of $f_{a2,a3}$ measurements are shown in Table II. As can be seen there, the expected precision on f_{a3} is in the range $0.03 - 0.04$, independent of the e^+e^- collision energy. This translates to very different constraints on $f^{\rm dec}_{a3}$ that range from 7×10^{-4} to 8×10^{-6}; as we already explained, measuring a similar fraction of events caused by the pseudoscalar anomalous couplings at higher energy means a sensitivity to a smaller value of g_4. The expected precision is therefore similar to what can be achieved from cross-section measurements at different energies, but in this case it relies on kinematic observables

rather than dynamic ones that can be subject to form-factor effects. The expected precision of $f_{a2}^{\rm dec}$ is comparable to that of $f_{a3}^{\rm dec}$. We also confirm that precision on f_{a3} does not change significantly if ϕ_{a3} is either floated or kept fixed provided that the measured value of f_{a3} is at least 3σ away from zero.

The process $e^+e^- \to ZH \to (\ell^+\ell^-)H$ is relatively simple and the three-dimensional (3D) analysis is sufficient to extract most information from the multi-parameter fit, as illustrated above. However, let us discuss this example as an illustration of how *CP*-analysis can be performed in other, more complicated, channels at both proton and lepton colliders. In $e^+e^- \to ZH$ dynamic information sensitive to form factors is contained in the $\sqrt{s}$ dependence and can be easily separated from the rest. The other two pieces of information, as we discussed above, can be incorporated in two discriminants D_{0^-} and D_{CP}, see Fig. 7 and Appendix B. The D_{0^-} discriminant is optimal to separate amplitudes squared representing the scalar and pseudoscalar contributions. The D_{CP} discriminant is optimal to separate interference of the scalar and pseudoscalar amplitudes.

The D_{CP} is particularly interesting as it incorporates the full information about interference in a single observable which exhibits clear forward-backward asymmetry indicating *CP* violation. There is a built-in assumption about the relative phase of the g_1 and g_4 terms in the D_{CP} construction. Under the assumption $\phi_{a3} = 0$ or π, which can be justified if heavy particles generate the g_4 coupling perturbatively, D_{CP} exhibits maximal forward-backward asymmetry, with the sign changing between $\phi_{a3} = 0$ and π. Should the phase be between 0 and π, the asymmetry is reduced and, eventually, vanishes at $\phi_{a3} = \pi/2$. If this happens, it is possible to construct another discriminant $D_{CP}^{\perp}$ that has maximal asymmetry at $\phi_{a3} = \pm\pi/2$ and has asymmetry vanishing at $\phi_{a3} = 0, \pi$. At any rate, it is straightforward to introduce the two discriminants (D_{CP}, $D_{CP}^{\perp}$) that will allow us to measure non-zero interference and the phase ϕ_{a3}.

We stress that it is advantageous to use D_{0^-} and D_{CP} discriminants. Indeed, they cleanly separate information contained either in the yields of *CP*-odd and *CP*-even contributions or their interference. The same information is present in the angular observables, such as those shown in Fig. 3, but it is hidden in the multi-dimensional space. For example, forward-backward asymmetry is also visible in the plots in Fig. 3, but it is less obvious in some cases. For example, in case of $\phi_{a3} = 0$ no simple observable exists to illustrate it. It is also hard to describe distributions with larger number of dimensions for some of the other processes (e.g. VBF discussed later) or to parameterize both the detector effects and background. It is relatively simple to parameterize the one- or two-dimensional distributions of D_{0^-} and D_{CP} as we show below. Moreover, this approach can be easily extended to measure f_{a2} using the dedicated discriminants with the same approach, which includes interference of the g_1 and g_2 terms.

Figure 7 illustrates the results of several measurements using either an optimal 3D analysis, or a single- or double-discriminant analysis. We omit background events in this study to simplify presentation, but this has little effect on the conclusion. For the discriminant parameterization, we use Eq. (B2) with either 1D or 2D template histograms. When f_{a3} is obtained from a one-dimensional fit to D_{0^-}, which does not contain an interference between the *CP*-odd and *CP*-even contributions, the precision on f_{a3} gets worse by about 65% with $f_{a3} = 0.05$, 37% with $f_{a3} = 0.10$ and by 12% with $f_{a3} = 0.50$ at $\sqrt{s} = 250$ GeV, with each case corresponding to 3σ measurements of f_{a3}. Note that interference scales as $\sqrt{f_{a3}}$ and therefore dominates at small values of f_{a3}. Hence, especially for small event fractions, the interference effects are important to include when non-zero *CP*-odd contribution is observed, and they appear to be more important in this mode than in the $H \to ZZ$ decay, as we will see below, because analysis does not rely on observables sensitive to dynamics. When f_{a3} is obtained from a two-dimensional fit of D_{0^-} and D_{CP}, precision of the full multi-dimensional fit is recovered. However, we note that D_{CP} or $D_{CP}^{\perp}$ do not provide additional constraint on f_{a3} without constraints on ϕ_{a3}.

All the above techniques can be applied to all other channels under consideration, as discussed below. While we provide the tools to explore all these methods, we often choose the more practical ways to illustrate expected precision in each channel.

B. The $H \to ZZ^*$ process on LHC

In this subsection, we study precision on tensor coupling measurements that can be achieved by exploiting kinematics of $H \to ZZ^*$ process at the LHC. The signal contributions are listed in Table I; we consider the sum of all five production mechanisms. The effective number of background events is estimated to be 0.4 times the number of signal events; it is modeled with the $q\bar{q} \to ZZ^*/Z\gamma^*$ process. We compare the sensitivity that can be reached when 300 fb^{-1} and 3000 fb^{-1} of integrated luminosity is collected at the LHC. The number of Higgs events at 300 fb^{-1} is taken to be 10% of the 3000 fb^{-1} yields quoted in Table I. Cross-sections for some of the simulated signal samples are listed in Table II.

Figure 8 (two left plots) illustrates precision on f_{a3} that can be achieved when both f_{a3} and ϕ_{a3} are allowed to float in the multi-parameter fit with seven observables. In that case generated values for $f_{a3} = 0.18$ (0.06) at 300 (3000) fb^{-1} are about three standard deviations away from zero. A similar approach is taken for precision in the f_{a2}

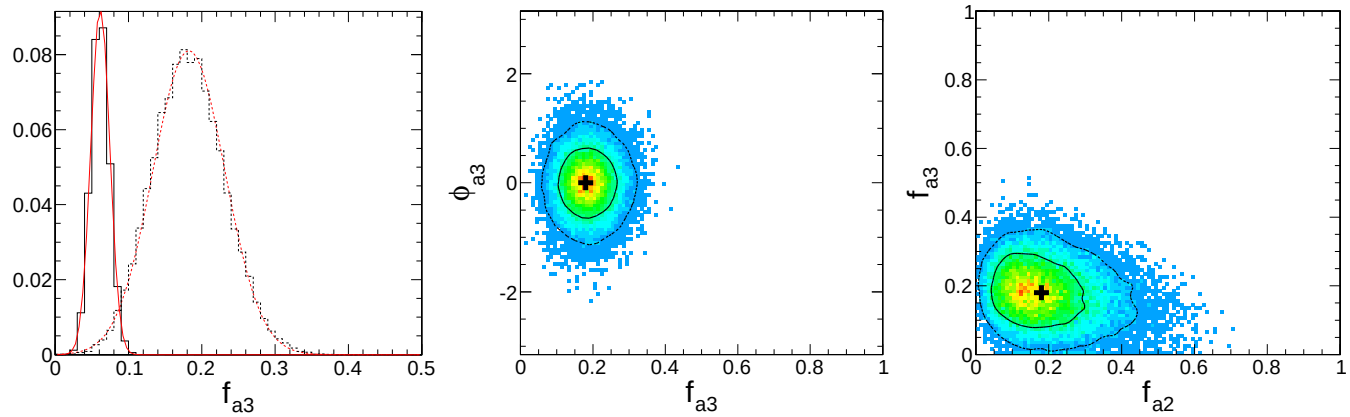

FIG. 8: Distribution of fitted values of f_{a3}, ϕ_{a3}, and f_{a2} in a large number of generated experiments in the $H \to ZZ^* \to 4\ell$ channel with 300 fb^{-1} of data collected at the LHC. Left plot: f_{a3} results from simultaneous fit of f_{a3} and ϕ_{a3} with 300 fb^{-1} (dotted) and 3000 fb^{-1} (solid). Middle and right plots: simultaneous fit of f_{a3} and ϕ_{a3} or f_{a3} and f_{a2}, with 68% and 95% confidence level contours shown.

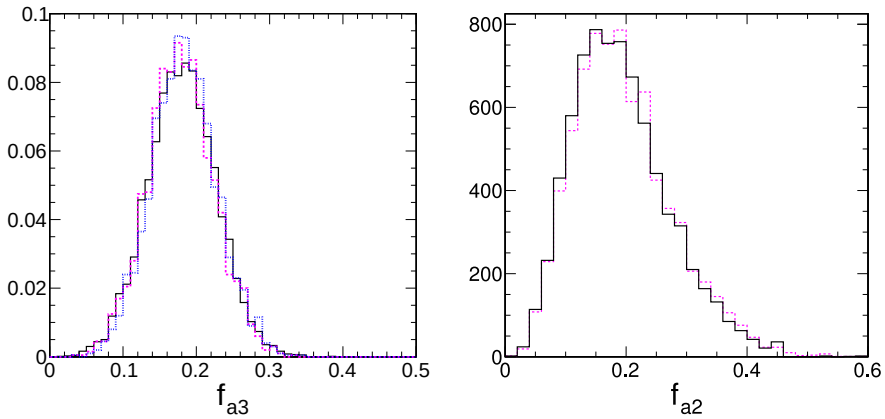

FIG. 9: Distribution of fitted values of f_{a3} and f_{a2} in a large number of generated experiments in the $H \to ZZ^* \to 4\ell$ channel with 300 fb^{-1} of data collected at the LHC, with background and detector effects not considered. Left plot: f_{a3} results with 1D fit of the D_{0^-} distribution (solid black); 7D fit with f_{a3} and ϕ_{a3} unconstrained (dotted blue); and 7D fit with f_{a3} only unconstrained (dashed magenta). Right plot: f_{a2} results with 1D fit of the D_{0h^+} distribution (solid black) and 7D fit (dashed magenta).

measurement, where for illustrative purpose we study the $\phi_{a2} = 0$ case. These results are summarized in Table II. We also show that both f_{a2} and f_{a3} could be measured simultaneously, see the third plot in Fig. 8. Overall, the expected precision on f_{a3} is 0.06 (0.02) with 300 (3000) fb^{-1} at the LHC, which is in good agreement with similar studies performed by CMS [46]. The expected precision on f_{a2} is comparable, but it more strongly depends on the phase ϕ_{a2} than in the case of f_{a3} measurement.

To study certain features of the multi-dimensional distributions, no background or acceptance effects were included for simplicity of the presentation. We do this, in particular, when we show results of the fits obtained in three different ways – one-dimensional fit of D_{0^-} with f_{a3} unconstrained, multi-dimensional fit with f_{a3} and ϕ_{a3} unconstrained, and multi-dimensional fit with f_{a3} unconstrained and ϕ_{a3} fixed to generated value. Figure 9 shows results of these fits assuming the 300 fb^{-1} luminosity at the LHC. The events were generated with $f_{a3} = 0.18$. We find f_{a3} precision to be essentially the same if ϕ_{a3} is either floated or constrained provided, of course, that the number of events is sufficiently high. When the one-dimensional fit of D_{0^-} is employed the precision of the f_{a3} measurement gets worse by about 4% with $f_{a3} = 0.18$ (3σ observation at 300 fb^{-1}), 13% with $f_{a3} = 0.06$ (3000 fb^{-1}) and 30% with $f_{a3} = 0.02$ (30000 fb^{-1}). This again illustrates our assessment that interference effects are important to include when non-zero *CP* contribution is observed *but* that they are not the primary drivers of the discovery of *CP* violation in HVV interactions with available statistics. Also shown in Fig. 9 are results of the f_{a2} fits where the 1D fit of the D_{0h^+} distribution and the full 7D fit with phase constrained are compared and show similar performance with statistics equivalent to 300 fb^{-1}.

C. The VBF process on LHC

We illustrate analysis of the weak boson fusion process considering two decays of the Higgs boson, $H \to ZZ^*$ and $H \to \gamma\gamma$. In both cases, two high transverse momentum jets are required. Yields of signal events are summarized in Table I. The $f_{\rm jet}$ parameter indicates the fraction of events with two jets. We ignore the VH production of Higgs bosons in this analysis since it can be isolated from the WBF events by applying cuts on the invariant mass of the two jets. We discuss VH production in the next subsection.

The gluon fusion production of a Higgs boson contaminates WBF sample significantly and is treated as a background. As shown below, *CP* properties of events produced in gluon fusion do not affect their kinematics strongly; this allows us to use the SM predictions for $pp \to H + 2j$ in the background studies. The other background originates from di-boson production with associated jets $ZZ(\gamma\gamma) + 2$ jets and is modeled explicitly in the analysis. Selection requirements follow closely those suggested by the ATLAS and CMS collaborations [5, 6]. In the analysis of the $H \to \gamma\gamma$ channel, additional requirements are applied on the dijet invariant mass $m_{jj} > 350$ GeV and pseudorapidity difference $\Delta\eta_{jj} > 3.5$, to improve the purity of the WBF signal. This leads to an additional WBF signal suppression by a factor 0.6 with respect to that quoted in Table I. The ratio of gluon fusion and weak boson fusion events is 0.42 and the ratio of di-boson + 2 jets and weak boson fusion events is 4.7 in the $H \to \gamma\gamma$ channel. The same ratios in the VBF $H \to ZZ^*$ channel are 2.2 and 0.7, respectively.

Analysis is performed with the two discriminants $\vec{x}_i = (D_{0^-}, D_{\rm bkg})$, as discussed in Appendix B. The D_{0^-} discriminant is sensitive to ratios of scalar to pseudoscalar components in the HVV vertex and is based on numerical matrix elements for two types of signals. The $D_{\rm bkg}$ discriminant is constructed to facilitate signal-to-background separation, where signal is represented by the scalar weak boson fusion matrix element, and background is represented by the scalar $H + 2j$ matrix element. Results of one-parameter fits of f_{a3} in both topologies are shown in Fig. 10 and presented in Table II. The $H \to ZZ$ channel is cleaner, but the $H \to \gamma\gamma$ channel provides higher statistics and, as a result, it has about three times better precision for the same collected luminosity. The ultimate precision on f_{a3} is in general comparable to that achieved in $H \to ZZ$ decay. However, due to large off-shell mass of the V^* in production, this translates to a substantially better precision on $f_{a3}^{\rm dec}$ of 1.3×10^{-4} with 3000 fb^{-1}.

It is interesting to reverse the analysis and search for *CP* violation in the gluon fusion production process. Since the selection requirements in the $H \to \gamma\gamma$ channel suppress gluon fusion production significantly, we investigate the feasibility of this measurement in the cleaner $H \to ZZ^*$ channel. The $D_{\rm bkg}$ discriminant remains the same, but it now serves the purpose to separate $H + 2$ jets signal from the SM weak boson fusion contamination. The D_{0^-} discriminant provides separation between production of scalar and pseudoscalar Higgs in gluon fusion events, based on the corresponding matrix elements. Results of this study are also shown in Fig. 10 and Table II. With 3000 fb^{-1}, the precision on f_{a3} is about 0.16, while with 300 fb^{-1} the precision is about 0.5.

An important consideration in the high-luminosity scenario of the LHC is a very high number of multiple proton-proton interactions per collision, leading to so-called pile-up events. The pile-up results in a very large number of relatively low p_T jets from multiple interactions which could fake a signal. There are detector design considerations which may improve suppression of such jets in data analysis. However, for the purpose of this study we mitigate the effects of increased pile-up in the 3000 fb^{-1} scenario by imagining that low-p_T jets cannot be reconstructed and by increasing p_T threshold for reconstructed jets to 50 GeV. As a consequence, the uncertainty on f_{a3} increases by 17% and 40% in the channels $V^*V^* \to H$ and $gg \to H + 2$ jets with $H \to ZZ^*$, respectively, while there is no noticeable change in $V^*V^* \to H \to \gamma\gamma$ due to tighter selection requirements. The changes are not dramatic and could be offset by other improvements in analyses, such as addition of other modes.

D. The $q\bar{q}' \to VH$ process on LHC

We illustrate analysis of VH events using two processes, $pp \to ZH/WH \to (q\bar{q}')(ZZ^*)$ and $pp \to ZH \to (\ell\ell)(b\bar{b})$. In the first case, the final state is identical to the one in WBF analysis, described in Section IV C. Discussion of major background contributions can be found there. The distinguishing feature of the ZH/WH signal is the peak in the $Z/W \to 2$ jets invariant mass m_{jj} distribution whose width is dominated by detector resolution. Therefore, we separate the m_{jj} probability distribution from the signal description and parameterize it with an empirical Gaussian function. The rest of the matrix element squared is parameterized analytically as a function of $(m_{VH}, \cos\theta_1, \cos\theta_2, \Phi, Y)$ using Eq. (A3). We find kinematics of the ZH and WH events to be essentially identical, except for the small shift in m_{jj}. Therefore, the results are obtained by combining the ZH/WH channels under a single topology using the ZH model. Similarly to the VBF case described in the previous subsection, we perform a two-dimensional fit with the discriminant $\vec{x}_i = (D_{0^-}, D_{\rm bkg})$.

To discuss $pp \to ZH \to (\ell\ell)(b\bar{b})$ case, we estimate signal and background yields following ATLAS and CMS selection requirements [5, 6]. The expected number of signal events is shown in Table I. To suppress otherwise overwhelming

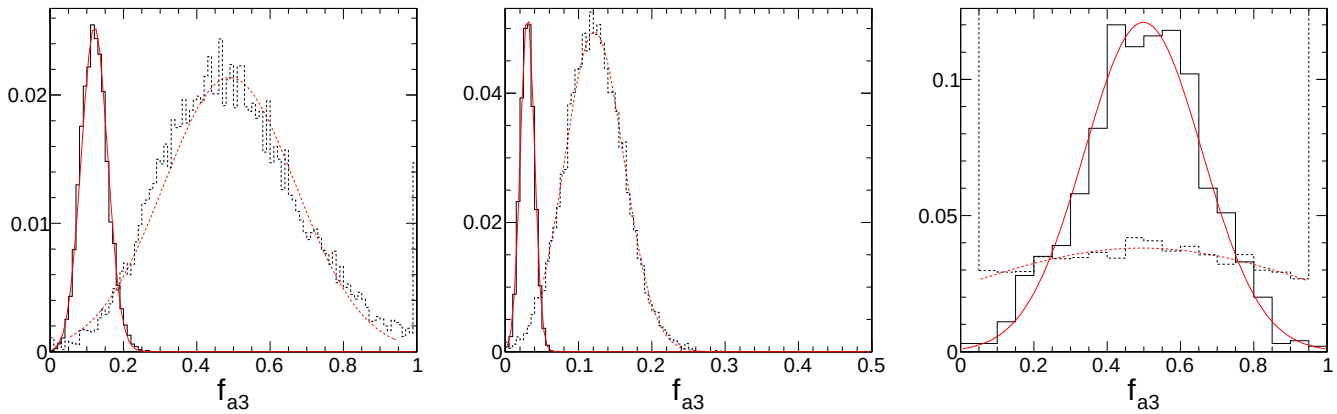

FIG. 10: Distribution of fitted values of f_{a3} in a large number of generated experiments in the weak boson fusion with $H \to ZZ^*$ (left) and $H \to \gamma\gamma$ (middle), and strong boson fusion with $H \to ZZ^*$ (right) channels with 300 fb^{-1} (dotted) and 3000 fb^{-1} (solid) of data collected at LHC.

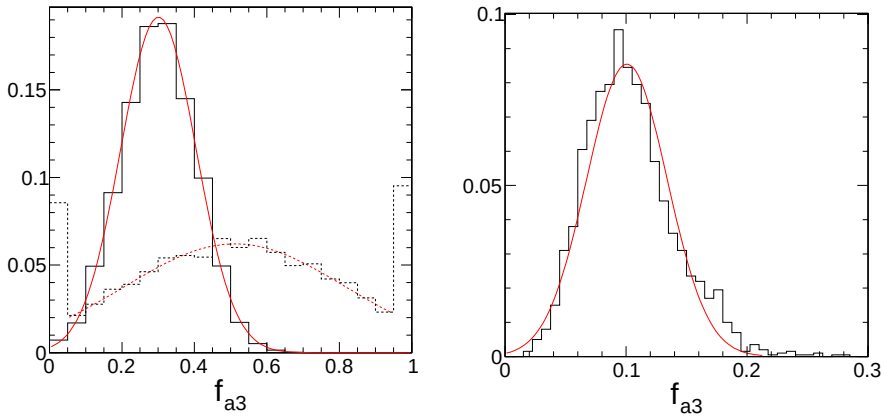

FIG. 11: Distribution of fitted values of f_{a3} in a large number of generated experiments in the channels $pp \to ZH/WH \to (q\bar{q}')(ZZ^*)$ (left) and $pp \to ZH \to (\ell\ell)(b\bar{b})$ (right) with 300 fb^{-1} (dotted) and 3000 fb^{-1} (solid) of data collected at the LHC.

background, we require large transverse momentum of the Higgs boson $p_{T,H} > 200$ GeV, see Fig. 4. This, combined with other selection requirements of the $Z \to \ell\ell$ and $H \to b\bar{b}$, leads to about 0.7% reconstruction efficiency. The dominant background is from Z+jets, which we take to be 5 times the size of signal with the above selection, but we approximate its shapes with $pp \to ZZ \to (\ell\ell)(b\bar{b})$ simulation. Approximate modeling of broad kinematic distributions does not affect separation between two types of signal. Analysis is performed in a narrow mass window of the $b\bar{b}$ invariant mass with a 1D $\vec{x}_i = (D_{0^-})$ parameterization using Eq. (A3) for probability calculations.

Results of one-parameter fits of f_{a3} using each of the two processes discussed above are shown in Fig. 11 and presented in Table II. The conclusion is very similar to the VBF topology study. The $H \to ZZ$ channel is cleaner, but the $H \to b\bar{b}$ channel provides higher statistics and as a result three times better precision for the same collected luminosity. The ultimate precision on f_{a3} is in general comparable to that achieved in $H \to ZZ$ decay. However, due to large off-shell mass of the Z^* in production, this translates to a substantially better precision on $f_{a3}^{\rm dec}$ defined in decay, 1.2×10^{-4} with 3000 fb^{-1}, similar to the expectation in the VBF channel. We mitigate the effects of increased pile-up in the 3000 fb^{-1} scenario by increasing thresholds of jet $p_T > 50$ GeV, which leads to about a factor of two degradation in precision in the $H \to ZZ$ channel. We note that the $H \to b\bar{b}$ channel has tighter selection requirements and could also benefit from jet substructure techniques [49].

V. SUMMARY AND CONCLUSIONS

In summary, we have investigated the feasibility to measure anomalous couplings of the Higgs boson to electroweak gauge bosons and gluons, including *CP*-violating couplings. A coherent framework is presented to study these anomalous couplings in Higgs decays, vector boson fusion, or associated production of a Higgs boson at either proton or lepton colliders. Both, a Monte Carlo simulation program and a matrix element likelihood approach are developed for these three types of processes. The expected sensitivity to the $f_{a3}^{\rm dec}$ parameter, defined as the *CP*-odd cross-section fraction in the decay to two vector bosons and which we will denote as f_{CP} here, is summarized in Table III and Fig. 12[1]. At both the high-luminosity LHC and the first stage of the e^+e^- collider, f_{CP} as small as 10^{-4} can be measured in the coupling to weak bosons (W and Z). Higher precision seems to be achievable at a higher-energy e^+e^- collider, provided that q^2-dependence of effective couplings does not yet lead to the suppression of non-renormalizable interactions.

The f_{CP} value in either $H \to ZZ$ or WW decay is expected to be small since the pseudoscalar coupling is loop-induced. Therefore, values as small as $f_{CP} \sim 10^{-5}$ might be expected even in the case of sizable admixture of a pseudoscalar. As follows from Table III, such small values cannot be measured either at the LHC or at the e^+e^- collider, but expected precision is not out of scale and interesting measurements could be achieved with higher luminosity and additional modes. Nonetheless, measuring f_{CP} in couplings to massless vector bosons ($gg, Z\gamma, \gamma\gamma$) might be an interesting alternative, since both scalar and pseudoscalar components are expected to be equally suppressed by the loop effect, and $f_{CP} \sim 10^{-2}$ might be expected [50]. We have tested the expected sensitivity to f_{CP} in the Hgg coupling at the LHC. We found that kinematic features in the production of the Higgs boson in the association with jets are not strongly modified but interesting measurements could be made with sufficient statistics.

Measuring f_{CP} in the $H \to Z\gamma$ and $H \to \gamma\gamma$ modes at the LHC is a challenge due to their low branching fractions, and it is essentially impossible at an e^+e^- collider. Nonetheless, the $H \to Z\gamma$ mode offers excellent kinematic distributions [26] to measure couplings from the angular correlations using the techniques similar to $H \to ZZ^*$, once sufficient signal sample is accumulated. We provide the tools to do so. The $H \to \gamma\gamma$ final states does not allow measurement of *CP* properties without the photon polarization measurement. The latter could be measured in photon conversion in the detector, but this makes the analysis very challenging and demands large statistics. Alternatively, there is a proposal for a photon collider which could be built in association with a linear e^+e^- collider and its strong feature is the ability to collide polarized photons, with which *CP* properties could be studied [51].

Finally, we comment on some further extensions of this analysis. First, similar measurements can be performed in $H \to WW^*$ decay mode. However, we have already shown [8] that spin-zero coupling measurement is less precise in this channel compared to $H \to ZZ^*$. Both decays could be studied at the e^+e^- collider, but the strongest feature of the e^+e^- collider is to measure these coupling in production, not in decay, due to larger statistics available and also

TABLE III: List of f_{CP} values in HVV couplings expected to be observed with 3σ significance and the corresponding uncertainties δf_{CP} for several collider scenarios, with the exception of $V^* \to VH$ mode at pp 300 fb^{-1} where the simulated measurement does not quite reach 3σ. Numerical estimates are given for the effective couplings Hgg, $H\gamma\gamma$, $HZ\gamma$, HZZ/HWW, assuming custodial Z/W symmetry and using HZZ couplings as the reference. The ✓ mark indicates that a measurement is in principle possible but is not covered in this study.

			HZZ/HWW						Hgg		$HZ\gamma$	$H\gamma\gamma$	
collider	energy	$\mathcal{L}$	$H \to VV^*$		$V^* \to VH$		$V^*V^* \to H$		$gg \to H$		$H \to Z\gamma$	$\gamma\gamma \to H$	$H \to \gamma\gamma$
	GeV	fb^{-1}	f_{CP}	δf_{CP}	f_{CP}	δf_{CP}	f_{CP}	δf_{CP}	f_{CP}	δf_{CP}			
pp	14 000	300	0.18	0.06	6×10^{-4}	4×10^{-4}	18×10^{-4}	7×10^{-4}	–	0.50			
pp	14 000	3 000	0.06	0.02	3.7×10^{-4}	1.2×10^{-4}	4.1×10^{-4}	1.3×10^{-4}	0.50	0.16	✓		✓
e^+e^-	250	250	✓		21×10^{-4}	7×10^{-4}	✓						
e^+e^-	350	350	✓		3.4×10^{-4}	1.1×10^{-4}	✓						
e^+e^-	500	500	✓		11×10^{-5}	4×10^{-5}	✓						
e^+e^-	1 000	1 000	✓		20×10^{-6}	8×10^{-6}	✓						
$\gamma\gamma$	125		✓									✓	

[1] The translation between the f_{a3} and $f_{a3}^{\rm dec} \equiv f_{CP}$ is not linear and may lead to asymmetric errors, from which we quote the uncertainty on the lower side. We omit the VH point at 300 fb^{-1} LHC scenario because it does not quite reach the 3σ threshold.

due to cross-section effects. Prospects for measuring anomalous couplings in the VBF process $Z^*Z^* \to H$ at an e^+e^- collider are similar to what we discussed at the LHC. The number of events in this mode is in fact much larger than in the $Z^* \to ZH$ production mode with $Z \to \ell\ell$ at higher energies [12], as shown in Table I. We leave further studies in this mode to future work, while the tools will be very similar to those already employed in LHC studies shown here.

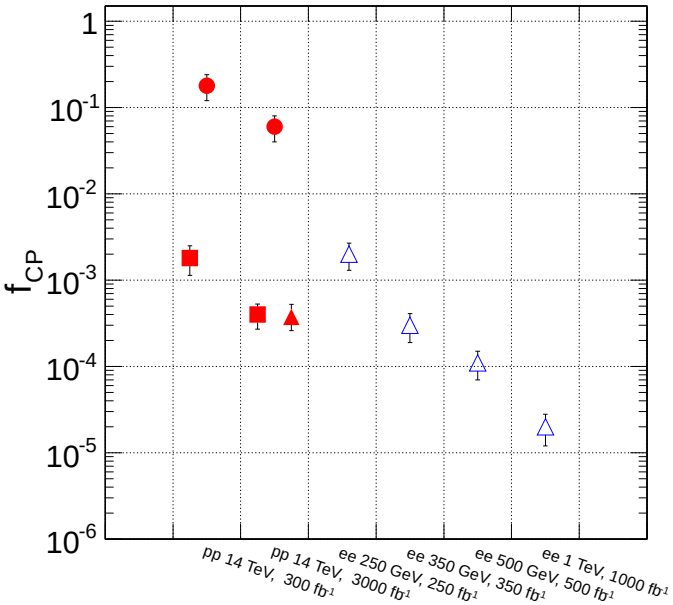

FIG. 12: Summary of precision in f_{CP} for HVV couplings ($V = Z, W$) at the moment of 3σ measurement. Points indicate central values and error bars indicate 1σ deviations in the generated experiments modeling different luminosity scenarios at proton (solid red) or e^+e^- (open blue) colliders. Measurements in three topologies VH (triangles), WBF (squares), and decay $H \to VV$ (circles) are shown. Different energy and luminosity scenarios are indicated on the x-axis.

Acknowledgments: We would like to acknowledge the long-term planning exercise for the US high-energy physics community, also known as "Snowmass," from which this study emerged. We would like to thank "Snowmass" participants and CMS collaboration colleagues for feedback, and in particular Michael Peskin and Tao Han for encouragement of the e^+e^- studies and Serguei Ganjour for discussion of the $\gamma\gamma$ channel on LHC. We are grateful to Jonathan Aguilar, Roberto Covarelli, Candice You, Xiaozhou Zhou for help with the generator validation. This research is partially supported by US NSF under grants PHY-1100862 and PHY-1214000, and by US DOE under grants DE-AC02-06CH11357 and DE-AC02-07CH11359. We also acknowledge support from the LPC-CMS Fellows program operated through FNAL. Calculations reported in this paper were performed on the Homewood High Performance Cluster of the Johns Hopkins University.

Appendix A: Event description with the matrix element likelihood approach

The main tool that we use in the analyses described in this paper is the likelihood method that employs expected probability distributions for various processes that can be used to measure anomalous Higgs boson couplings. In this Appendix, we provide the necessary information for finding these probability distributions and give a few examples of how they can be used.

1. The $H \to VV^*$ process

We begin by describing the decay process $H \to VV \to 4f$, following notation of Refs. [7, 8]. This process is important not only because it can be used directly to constrain anomalous couplings but also because various crossings of $H \to VV$ amplitude give amplitudes for associated Higgs boson production and vector boson fusion. Complete description of the decay amplitude for $H \to VV^*$ requires two invariant masses and five angles, defined in Fig. 1. We collectively denote these angles as $\vec{\Omega} = (\cos\theta^*, \Phi_1, \cos\theta_1, \cos\theta_2, \Phi)$. The probability distribution that describes the decay of a Higgs boson to two gauge bosons V is written as

$$\frac{d\Gamma(m_1, m_2, \vec{\Omega})}{dm_1\, dm_2\, d\vec{\Omega}} \propto |\vec{p}_V(m_1, m_2)| \times \frac{m_1^3}{(m_1^2 - m_V^2)^2 + m_V^2\Gamma_V^2} \times \frac{m_2^3}{(m_2^2 - m_V^2)^2 + m_V^2\Gamma_V^2} \times \frac{d\Gamma(m_1, m_2, \vec{\Omega})}{d\vec{\Omega}}\,, \qquad \text{(A1)}$$

where the fully analytical expression for $d\Gamma/d\vec{\Omega}$ is given in Eq. (A1) of Ref. [8], and $\vec{p}_V$ is the V boson momentum in H rest frame. We show examples of kinematic distributions obtained for different types of tensor couplings in Fig. 13. Simulated events and projections of analytic distributions from Eq. (A1) are compared there, illustrating an agreement between the two computations. Additional examples, including angular distributions for other spin hypotheses, can be found in Ref. [8]. We note that lepton interference in the final states with identical leptons changes the expected performance of the analysis by only a few percent. We therefore neglect this interference, but provide the tools to take it into account [37].

2. The $e^+e^- \to ZH$ process

We obtain the matrix element for the $e^+e^- \to Z^* \to ZH$ process by crossing the amplitudes for $H \to ZZ^*$ described above. Since the intermediate Z^* boson has fixed invariant mass[2] and all final state particles are on shell, the probability distribution depends on five angles $\vec{\Omega}$, defined in the middle pane of Fig. 1. It might be easier to

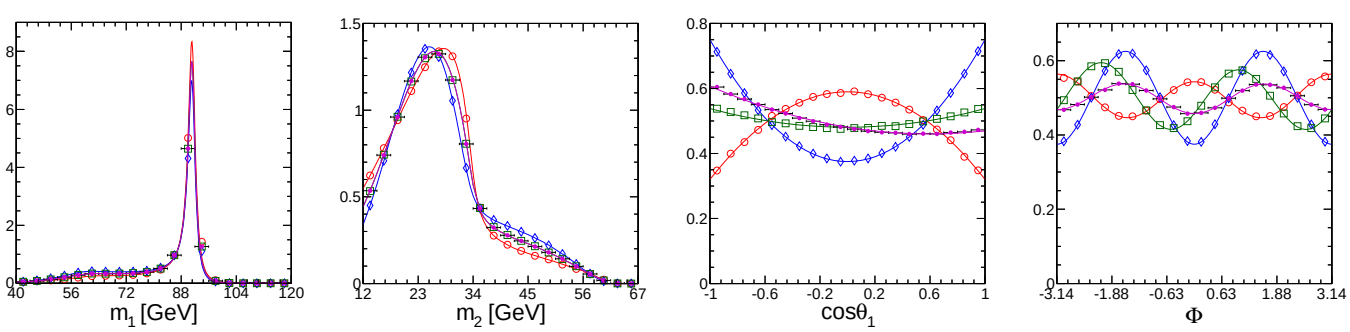

FIG. 13: Distributions of the observables in the $H \to ZZ$ analysis, from left to right: m_1, m_2 (where $m_1 > m_2$), $\cos\theta_1$ (same as $\cos\theta_2$), and Φ. Points show simulated events and lines show projections of analytical distributions. Four scenarios are shown: SM (0^+, red open circles), pseudoscalar (0^-, blue diamonds), and two mixed states corresponding to $f_{a3} = 0.5$ with $\phi_{a3} = 0$ (green squares) and $\pi/2$ (magenta points). For a spin-zero particle, distributions in $\cos\theta^*$ and Φ_1 are trivially flat, but this is not true for higher-spin states [8] or with detector effects.

[2] The invariant mass obviously coincides with the energy $\sqrt{s}$ of an e^+e^- collider.

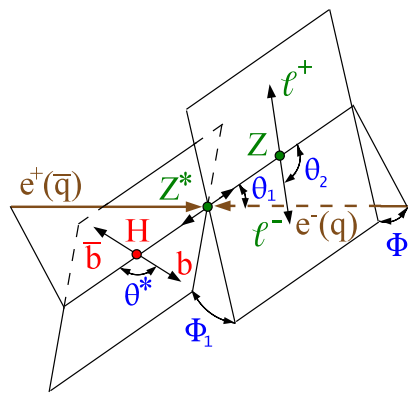

FIG. 14: Higgs production and decay at the e^+e^- or pp collider with $e^+e^-(q\bar{q}) \to Z^* \to ZH \to \ell^+\ell^- b\bar{b}$ as shown in the parton collision frame.

understand the decay kinematics in Fig. 14, but we would like to stress that the two are equivalent and Fig. 1 allows direct analogy with the already established process of a Higgs boson decay.

To compute the differential cross-section for $e^+e^- \to ZH \to \mu^+\mu^- H$, we modify $d\Gamma/d\vec{\Omega}$ in Eq. (A1) of Ref. [8] to account for changes in kinematics. In particular, $s' = q_1 q_2$ in Eq. (13) of Ref. [8][3] is defined for two outgoing momenta of Z-bosons. If instead we use the four-momentum P_1 of the initial e^+e^- state, we must write $q_1 = -P_1$ and, as a result, $s' = -P_1 q_2 = -(m_H^2 - m_1^2 - m_2^2)/2$, where $m_1^2 = P_1^2$ and $m_2^2 = m_Z^2$. This leads to the following differential angular distributions for a spin-zero particle production

$$\begin{aligned}\frac{d\Gamma_{J=0}(s,\vec{\Omega})}{d\vec{\Omega}} \propto\, & 4\,|A_{00}|^2\,\sin^2\theta_1 \sin^2\theta_2 \\ & + |A_{+0}|^2\left(1 - 2R_1\cos\theta_1 + \cos^2\theta_1\right)\left(1 + 2A_{f_2}\cos\theta_2 + \cos^2\theta_2\right) \\ & + |A_{-0}|^2\left(1 + 2R_1\cos\theta_1 + \cos^2\theta_1\right)\left(1 - 2A_{f_2}\cos\theta_2 + \cos^2\theta_2\right) \\ & - 4|A_{00}||A_{+0}|(R_1 - \cos\theta_1)\sin\theta_1(A_{f_2} + \cos\theta_2)\sin\theta_2\cos(\Phi + \phi_{+0}) \\ & - 4|A_{00}||A_{-0}|(R_1 + \cos\theta_1)\sin\theta_1(A_{f_2} - \cos\theta_2)\sin\theta_2\cos(\Phi - \phi_{-0}) \\ & + 2|A_{+0}||A_{-0}|\sin^2\theta_1\sin^2\theta_2\cos(2\Phi - \phi_{-0} + \phi_{+0})\,. \end{aligned} \tag{A2}$$

In Eq. (A2), $R_1 = (A_{f_1} + P^-)/(1 + A_{f_1}P^-)$, where $A_{f_i} = 2\bar{g}_V^f \bar{g}_A^f/(\bar{g}_V^{f2} + \bar{g}_A^{f2})$ is the parameter characterizing the decay $Z_i \to f_i \bar{f}_i$ [52] with $A_{f_1} \simeq 0.15$ for the Zee coupling, A_{f_2} is for the coupling to fermions in the Z decay, and P^- is the effective polarization of the electron beam defined in such a way that $P^- = 0$ corresponds to the unpolarized beam. Amplitudes $|A_{\lambda_1\lambda_2}|$ and their phases $\phi_{\lambda_1\lambda_2}$ are obtained by crossing the corresponding expressions in Eqs. (9)–(15) of Ref. [8]. Examples of kinematic distributions in the $e^+e^- \to ZH$ process can be found in Fig. 3; they show good agreement between analytical parameterization and numerical computations and exhibit features similar to those seen in decay in Fig. 13. Extension to higher spins follows the same logic and can be easily written using expressions in Ref. [8], such as Eqs. (A1), (17), (21). Applications to spin-zero, -one, and -two particle production can be found in Figs. 5 and 15.

3. The $q\bar{q}' \to VH$ process on LHC

To describe associated ZH and WH production in proton collisions we modify Eq. (A2) to account for the fact that we now have quarks and antiquarks colliding and that the energy and luminosity distribution of these partonic collisions is described by products of parton distribution functions. The probability distribution for $pp \to ZH$ and $pp \to WH$ processes is described by

$$\frac{d\Gamma(\hat{s}, Y, \vec{\Omega})}{d\hat{s}\,dY\,d\vec{\Omega}} \propto \sum_{q,\bar{q}'} \mathcal{P}_{q\bar{q}'}(\hat{s}, \vec{\Omega}) \times P(\hat{s}) \times F_{q\bar{q}'}(\hat{s}, Y)\,, \tag{A3}$$

[3] We add prime to s' to avoid confusion with $\sqrt{s} = m_1$ in this case.

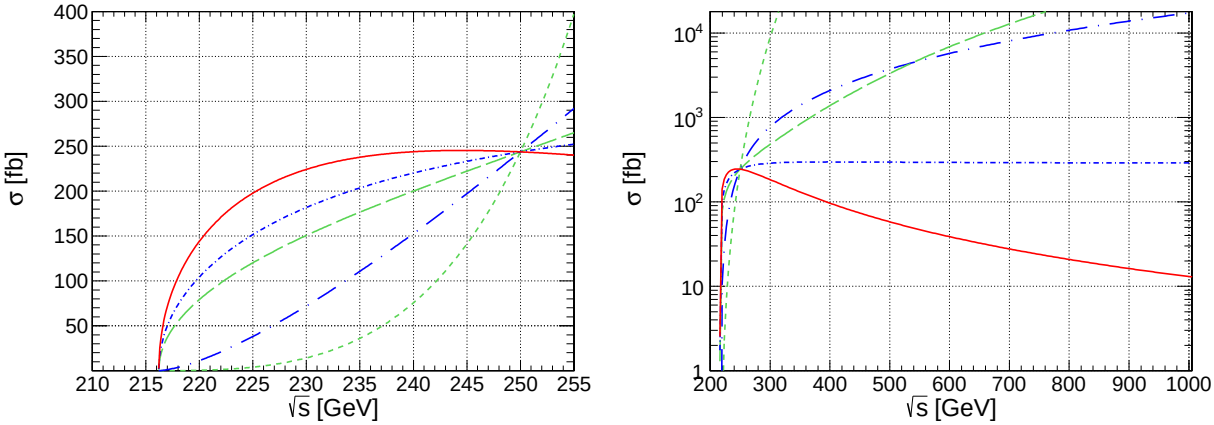

FIG. 15: Cross-section of $e^+e^- \to Z^* \to ZX$ process as a function of $\sqrt{s}$ for several representative models: SM Higgs (0^+, solid red), vector (1^-, dot-long-dashed blue), axial vector (1^+, dot-short-dashed blue), KK graviton with minimal couplings (2^+_m, long-dashed green), spin-2 with higher-dimension operators (2^+_h, short-dashed green). All cross-sections are normalized to SM value at $\sqrt{s} = 250$ GeV.

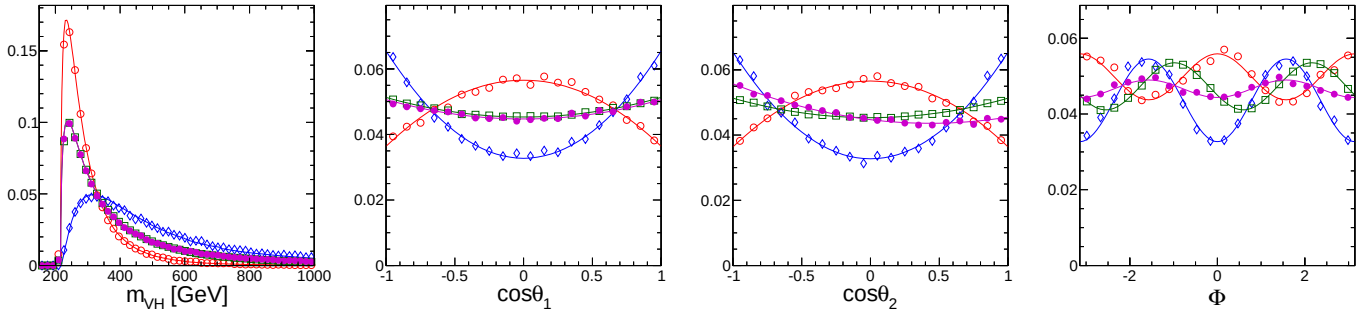

FIG. 16: Distributions of the observables in the $pp \to ZH$ analysis, from left to right: m_{VH}, $\cos\theta_1$, $\cos\theta_2$, Φ. Points show simulated events and lines show projections of analytical distributions. Four scenarios are shown: SM (0^+, red open circles), pseudoscalar (0^-, blue diamonds), and two mixed states corresponding to $f_{a3} = 0.5$ with $\phi_{a3} = 0$ (green squares) and $\pi/2$ (magenta points).

where the sum runs over the five $q\bar{q}$ flavors in the $Z^* \to ZH$ production and over 12 $q\bar{q}'$ flavors in the $W^* \to WH$ process, $\hat{s} = m^2_{VH}$, $\mathcal{P}_{q\bar{q}'}(\hat{s}, \vec{\Omega})$ is the amplitude squared from Eq. (A2), $P(\hat{s})$ is the kinematic factor [11], and $F_{q\bar{q}'}(\hat{s}, Y)$ is the partonic luminosity function

$$F_{q\bar{q}'}(\hat{s}, Y) = f_q(x_+, \hat{s}) f_{\bar{q}'}(x_-, \hat{s}) + (x_+ \leftrightarrow x_-)\,, \tag{A4}$$

where $x_\pm = \sqrt{\hat{s}/s}\, e^{\pm Y}$. All angular variables are defined in the partonic center-of-mass frame.

Sample kinematic distributions are shown in Fig. 16. There is a good agreement between numerical simulations and analytic probability distributions. We note that continuous distribution of the invariant mass $m_{VH} = \sqrt{\hat{s}}$ scans the range of a few hundred GeV which is in the ballpark of center-of-mass energies proposed for e^+e^- colliders.

4. Higgs production in association with two jets

For studies of the Higgs boson production in association with two jets for both weak boson fusion and gluon fusion see e.g. Ref. [16]. Analytic parameterization of the probability distribution in this case is more involved because the two vector bosons have negative virtualities $q_i^2 < 0$, and because parton distribution functions of a proton need to be incorporated. Although a partial analytic description of probability distributions is available, see e.g. Ref. [19], in this analysis we employ the matrix elements for $pp \to H + 2j$ as implemented in the JHU generator. In Fig. 17 we show representative distributions of di-jet observables m_{jj}, $\Delta\eta_{jj}$, $\Delta\phi_{jj}$, and the vector boson $\sqrt{|q_V^2|}$, for the scalar, pseudoscalar, and mixed states produced in weak boson fusion. The same distributions are shown in Fig. 18 for Higgs

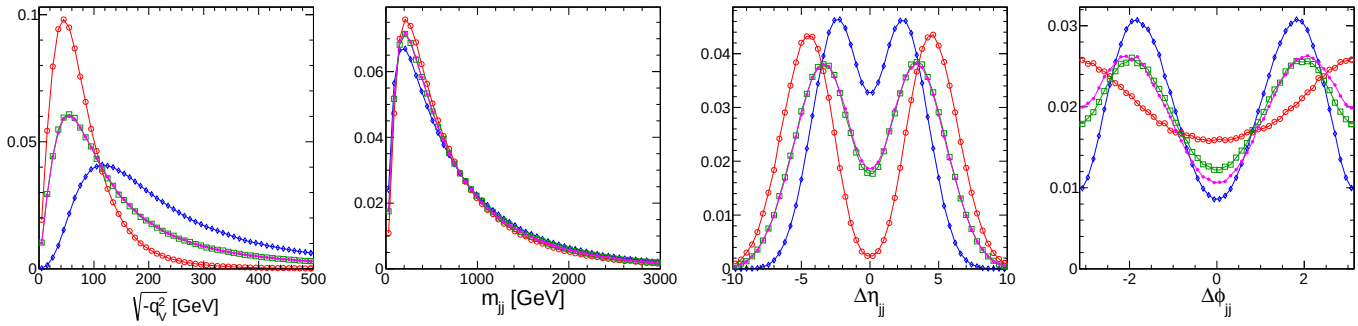

FIG. 17: Distributions of di-jet observables $\sqrt{-q_V^2}$, m_{jj}, $\Delta\eta_{jj}$, $\Delta\phi_{jj}$ in the weak vector boson fusion production of a 125 GeV Higgs boson at LHC with 14 TeV energy. Points connected by lines show simulated events. Four scenarios are shown: SM (0^+, red open circles), pseudoscalar (0^-, blue diamonds), and two mixed states corresponding to $f_{a3} = 0.5$ with $\phi_{a3} = 0$ (green squares) and $\pi/2$ (magenta points).

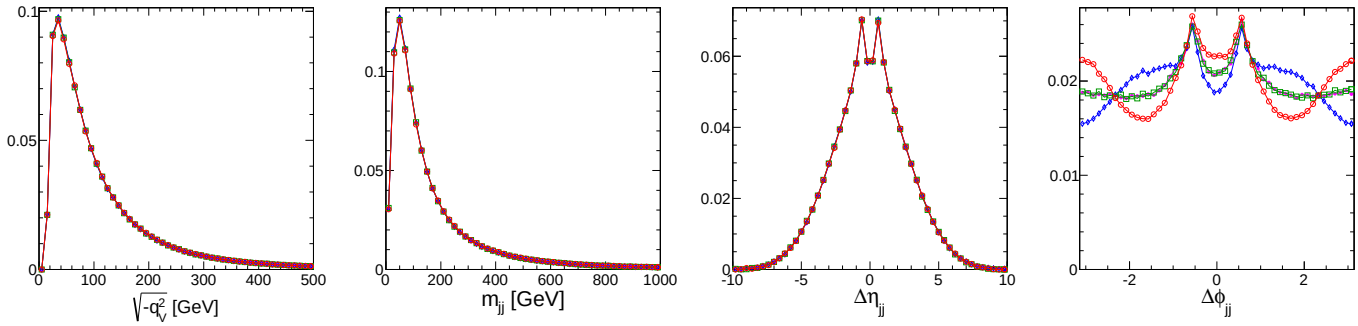

FIG. 18: Distributions of di-jet observables $\sqrt{-q_V^2}$, m_{jj}, $\Delta\eta_{jj}$, $\Delta\phi_{jj}$ in the strong vector boson fusion production of a 125 GeV Higgs boson at LHC with 14 TeV energy. Points connected by lines show simulated events. Selection requirements are applied on jets $p_T > 15$ GeV and $\Delta R_{jj} > 0.5$. Four scenarios are shown: SM (0^+, red open circles), pseudoscalar (0^-, blue diamonds), and two mixed states corresponding to $f_{a3} = 0.5$ with $\phi_{a3} = 0$ (green squares) and $\pi/2$ (magenta points).

boson production in gluon fusion. Several observables, in particular $\Delta\phi_{jj}$, exhibit differences between the scalar and pseudoscalar couplings. The enhanced production of events with anomalous couplings at higher values of $|q_i^2|$ in WBF is similar to the VH process; this effect is signficiantly weaker in the gluon fusion.

5. Background

Parameterization of background matrix elements is important for signal-to-background separation. Indeed, this was a crucial part of the Higgs boson discovery by the CMS collaboration [2] with the MELA technique which identifies kinematic differences between dilepton pairs produced in the decay of the Higgs boson via $H \to ZZ^* \to 4\ell$ and in $q\bar{q}$ annihilation, $q\overline{q} \to ZZ^*/Z\gamma^*$, to distinguish them from each other. We use MCFM [53] matrix elements for both $q\overline{q} \to ZZ^*/Z\gamma^*/Z\gamma$ and $gg \to ZZ^*$ processes to describe relevant backgrounds [37]. We also provide interference of $gg \to ZZ^*$ [53] and $gg \to H^* \to ZZ$ [37] for optimal analysis above the ZZ threshold, such as a study suggested in Refs. [54, 55]. We note that analytic parameterization of the $q\bar{q} \to ZZ^*/Z\gamma^*$ background is also available [31] and we also use it for the background parameterization. A similar approach to $q\bar{q} \to ZZ^*/Z\gamma^*$ background is also discussed in Ref. [56].

6. Analytic parameterization of parton distribution functions

Calculation of both signal and background processes at a hadron collider involves parton distribution functions (PDFs). These functions are usually calculated numerically by solving Altarelli-Parisi equations using dedicated numerical programs. It may be desirable, in some cases, to have an analytic parameterization of the parton distribution functions. For example, such parameterization may allow faster computations or even analytic integrations of the products of PDFs and partonic cross-sections. Parton distribution functions $f_q(x, \hat{s})$ are extracted from CTEQ6 PDF

set [57, 58] and are parameterized analytically using polynomial and exponential functions in the relevant range of x with coefficients that are also functions of $\hat{s}$ [59, 60]. The resulting set of analytically-parameterized CTEQ6L1 PDFs can be found in Ref. [37]. The partonic luminosity functions from Eq. (A4) are shown in Fig. 19.

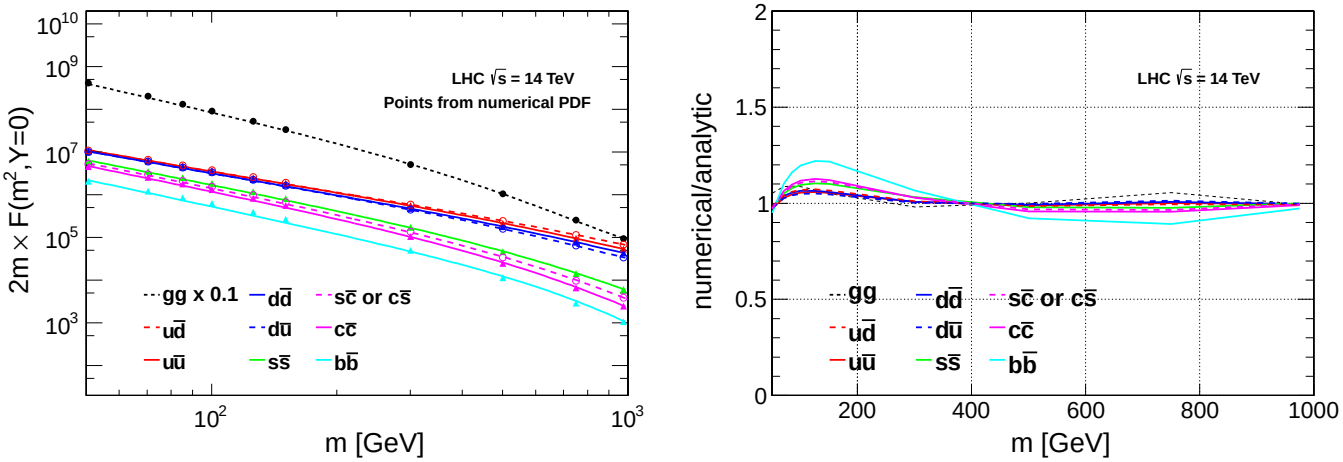

FIG. 19: Distribution of $2mF_{q\overline{q}'}(m^2, Y=0)$ defined in Eq. (A4) for proton-proton collision energies of 14 TeV as a function of the parton invariant mass m. On the left plot, curves show analytical approximation and points show exact numerical calculation using CTEQ6L1 PDFs. On the right plot, ratio between the numerical and analytical parameterizations is shown. CKM-suppressed $q\overline{q}'$ combinations are not shown. An equivalent factor for gluon-fusion production is shown for comparison and is scaled by a factor of 0.1.

Appendix B: Statistical Approaches

The ultimate goal of the analysis described in this paper is the measurement of all anomalous couplings of the Higgs bosons to the gauge bosons. This can be accomplished by performing a multi-dimensional fit to match observed kinematic distributions in various processes to theory predictions. Theoretical input to the fit involves real parameters $\vec{\zeta} = \{f_{a2}, f_{a3}, \phi_{a2}, \phi_{a3}\}$ in Eq. (2) which, once known, can be used to derive the couplings. To set up a fit process, we follow Ref. [7] and introduce the likelihood function for N candidate events

$$\mathcal{L} = \exp\left(-n_{\rm sig} - n_{\rm bkg}\right) \prod_i^N \left(n_{\rm sig} \times \mathcal{P}_{\rm sig}(\vec{x}_i;\ \vec{\zeta}) + n_{\rm bkg} \times \mathcal{P}_{\rm bkg}(\vec{x}_i) \right) , \tag{B1}$$

where $n_{\rm sig}$ is the number of signal events, $n_{\rm bkg}$ is the number of background events, and $\mathcal{P}(\vec{x}_i; \vec{\zeta})$ is the probability density function for signal or background. Each candidate event i is characterized by a set of eight observables, for example $\vec{x}_i = \{m_1, m_2, \vec{\Omega}\}_i$ as defined in Fig. 1. The number of observables and free parameters can be extended or reduced, depending on the desired fit.

The advantage of this approach is that the likelihood $\mathcal{L}$ in Eq. (B1) can be maximized for a large set of parameters in the most optimal way without losing information. The disadvantage is the difficulty to describe the detector response and background parameterization in a multi-dimensional space. In addition, convergence of the fit for a limited number of events may be an issue as well.

Nonetheless, successful implementation can be achieved with certain approximations, for example by allowing for a single anomalous coupling constant at a time. Consider a case where f_{a3} and ϕ_{a3} are non-vanishing and write the signal probability as

$$\mathcal{P}_{\rm sig}(\vec{x}_i; f_{a3}, \phi_{a3}) = (1 - f_{a3})\, \mathcal{P}_{0^+}(\vec{x}_i) + f_{a3}\, \mathcal{P}_{0^-}(\vec{x}_i) + \sqrt{f_{a3}(1 - f_{a3})}\, \mathcal{P}_{\rm int}(\vec{x}_i; \phi_{a3}) , \tag{B2}$$

where $\mathcal{P}_{\rm int}$ describes interference of 0^+ (g_1) and 0^- (g_4) terms.

In this simplified approach, we consider a single observable $\vec{x}_i = \{D_{0^-}\}_i$ and one free parameter $\vec{\zeta} = \{f_{a3}\}$. A kinematic discriminant is constructed from the ratio of probabilities for the SM signal and alternative signal 0^-

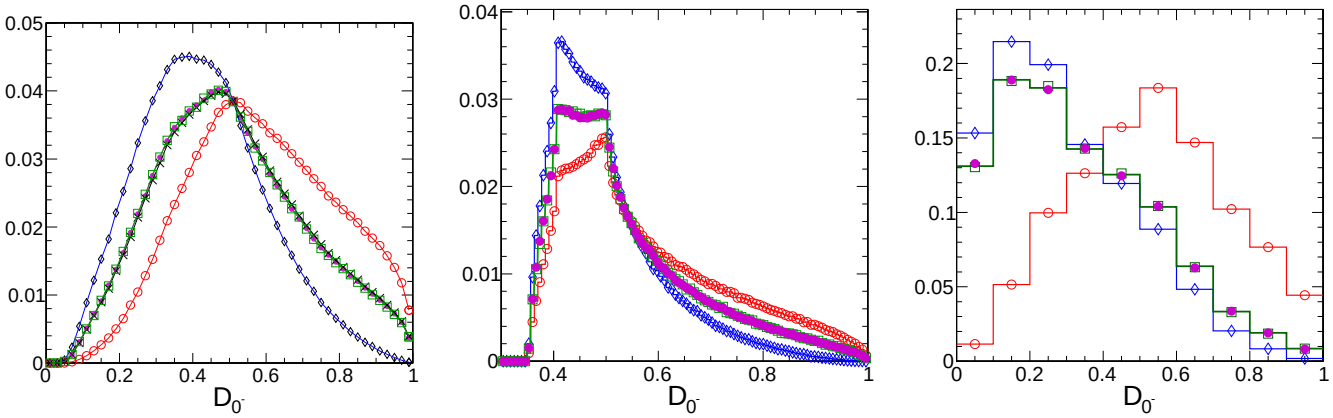

FIG. 20: Distribution of D_{0^-} for generated events in three topologies: $H \to ZZ \to 4\ell$ (left), $e^+e^- \to Z^* \to ZH \to (\ell\ell)(b\bar{b})$ (middle) at $\sqrt{s} = 250$ GeV, and $q\bar{q} \to Z^* \to ZH \to (\ell\ell)(b\bar{b})$ (right) at a 14 TeV pp collider. Four processes are shown: SM scalar (0^+, red open circles), pseudoscalar (0^-, blue diamonds), and two mixed states corresponding to $f_{a3} = 0.5$ with $\phi_{a3} = 0$ (green squares) and $\pi/2$ (magenta points). Also shown is the $f_{a3} = 0.5$ sample with no interference between the scalar and pseudoscalar terms simulated (black crosses). Events are shown after selection requirements, which have different efficiencies for 0^+ and 0^- samples in the $q\bar{q} \to Z^* \to ZH$ channel.

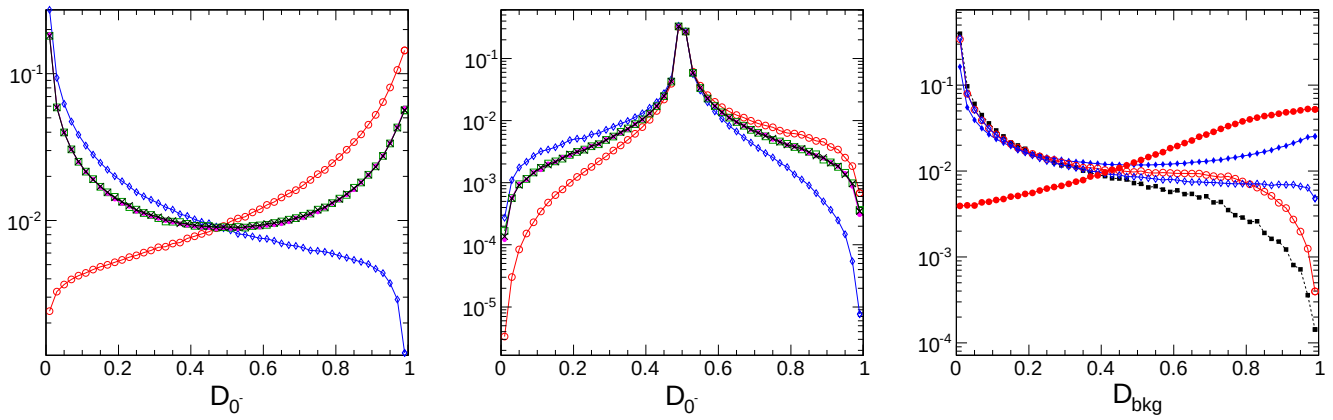

FIG. 21: Distribution of D_{0^-} for generated events in two VBF-like topologies: $V^*V^* \to H + 2$ jets (left) and $gg \to H + 2$ jets (middle), with $H \to ZZ^*$ as an example. Four processes are shown: SM (0^+, red open circles), pseudoscalar (0^-, blue diamonds), and two mixed states corresponding to $f_{a3} = 0.5$ with $\phi_{a3} = 0$ (green squares) and $\pi/2$ (magenta points). Also shown is the $f_{a3} = 0.5$ sample with no interference between the scalar and pseudoscalar terms simulated (black crosses). Right: Distribution of $D_{\rm bkg}$ for VBF topology considering $V^*V^* \to H + 2$ jets as signal and $gg \to H + 2$ jets as background. The following processes are shown: WBF 0^+ (red solid circles), WBF 0^- (blue solid diamonds), SBF 0^+ (red open circles), SBF 0^- (blue open diamonds), $ZZ + 2$ jets background (black squares). Events are shown after selection requirements.

hypothesis

$$D_{0^-} = \frac{\mathcal{P}_{0^+}}{\mathcal{P}_{0^+} + \mathcal{P}_{0^-}} = \left[1 + \frac{\mathcal{P}_{0^-}(m_1, m_2, \vec{\Omega})}{\mathcal{P}_{0^+}(m_1, m_2, \vec{\Omega})}\right]^{-1} . \tag{B3}$$

We now make a technical comment that allows us to simplify fitting for f_{a3} when distribution of D_{0^-} is employed. Consider a *CP*-mixed case. The matrix element squared, which is used to generate events for the D_{0^-} distribution, contains the square of *CP*-even part, the square of *CP*-odd part, and the interference of the two, as shown in Eq. (B2). We observe that the interference part does not contribute to the distribution of D_{0^-} variable; the illustration for five production and decay processes considered in this paper can be found in Figs. 20 and 21. This allows us to set up a simple procedure by generating f_{a3}-independent *CP*-even and *CP*-odd events *once* and then combining them in appropriate proportion. This feature is unique for f_{a3} measurements. As long as only a limit is set on f_{a3}, such an analysis may be sufficient. Note that this approach is equivalent to averaging over all possible phases of the amplitude,

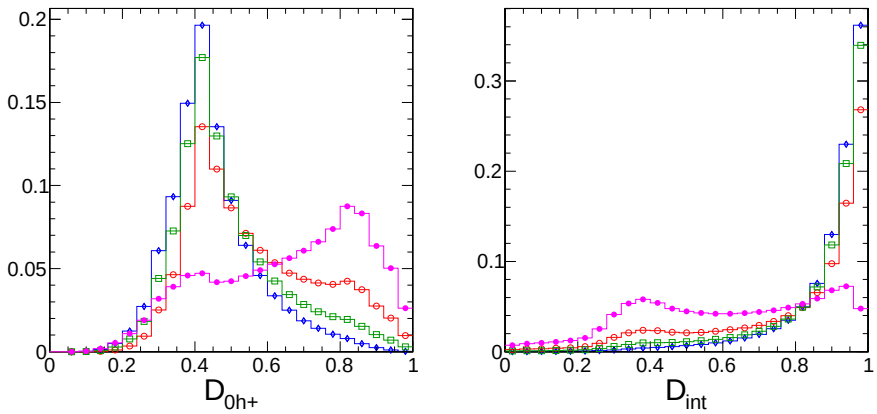

FIG. 22: Distribution of D_{0h^+} (left) and $D_{\rm int}$ (right) for generated events in the $H \to ZZ \to 4\ell$ process. Four scenarios are shown: SM scalar (0^+, red open circles), BSM scalar (0^+_h, blue diamonds), and two mixed states corresponding to $f_{a2} = 0.5$ with $\phi_{a2} = 0$ (green squares) and π (magenta points).

ϕ_{a3}, which is generally unknown until measured.

It is possible to extend the above approach and create a discriminant, D_{CP}, which is sensitive to interference of the 0^+ (g_1) and 0^- (g_4) terms

$$D_{CP} = \frac{\mathcal{P}_{\rm int}(m_1, m_2, \vec{\Omega})}{\mathcal{P}_{0^+}(m_1, m_2, \vec{\Omega}) + \mathcal{P}_{0^-}(m_1, m_2, \vec{\Omega})} \,. \tag{B4}$$

This analysis includes two observables $\vec{x}_i = \{D_{0^-}, D_{CP}\}_i$ and one parameter $\vec{\zeta} = \{f_{a3}\}$ for a given value of ϕ_{a3}. Such an approach can be also applied to other cases, such as a measurement of the parameter f_{a2}, where the $\mathcal{P}_{\rm int}$ cannot be omitted. The corresponding discriminants are called D_{0h^+} and $D_{\rm int}$, instead of D_{0^-} and D_{CP}; their distributions are shown in Fig. 22. The strong interference effect is visible in Fig. 22 and the full treatment Eq. (B2) is needed.

Background treatment requires special consideration. The set $\vec{x}_i$ can be extended to include observables discriminating against background, such as reconstructed Higgs boson invariant mass. For studies presented here, we adopt a simplified approach where instead of including Higgs boson invariant mass we fix the number of background events $n_{\rm bkg}$ to expected yields. Nonetheless, in some cases an effective background suppression can be achieved with a matrix element approach as well. In such a case we employ a second discriminant optimal for background suppression

$$D_{\rm bkg} = \left[1 + \frac{\mathcal{P}_{\rm bkg}(m_1, m_2, \vec{\Omega})}{\mathcal{P}_{0^+}(m_1, m_2, \vec{\Omega})}\right]^{-1} \tag{B5}$$

and extend the set of observables to include $\vec{x}_i = \{D_{0^-}, D_{\rm bkg}\}_i$. We note that this is needed only in the simplified approach employing discriminants. In the case of multidimensional fits, complete kinematic information is already contained in the set of observables.

To illustrate the use of $D_{\rm bkg}$, we show the separation of the gluon-fusion "background" and the weak-boson "signal" in $H + 2j$ events in Fig. 21. A similar approach can be used in the analysis of VH production with the decay $V \to 2$ jets, where the gluon fusion process $H + 2$ jets is treated as a background. Alternatively, extraction of f_{a3} in gluon fusion should treat the WBF process as a background.

The above approaches with kinematic discriminants simplify parameterization of detector effects and backgrounds. The full multi-parameter implementation in Eq. (B1) requires parameterization of detector effects. For the final states with leptons, the resolution effects are typically small and can be ignored for most of the observables. When such effects become important, detector transfer functions between the ideal and the reconstructed observables can in principle be incorporated into the probability distributions. The non-uniform reconstruction efficiency can be modeled with the acceptance function $\mathcal{G}$ which enters the $\mathcal{P}_{\rm sig}$ parameterization and is given by the step-function

$$\mathcal{G}(m_1, m_2, \vec{\Omega}) = \prod_\ell \theta(|\eta_{\rm max}| - |\eta_\ell(m_1, m_2, \vec{\Omega})|) \,, \tag{B6}$$

where $\eta_\ell = \ln\cot(\theta_\ell/2)$ is the pseudorapidity of a lepton and $|\eta_{\rm max}|$ is the maximal pseudorapidity in reconstruction. We also assume that the detection efficiency does not change within the detector acceptance, otherwise $\mathcal{G}$ is multiplied

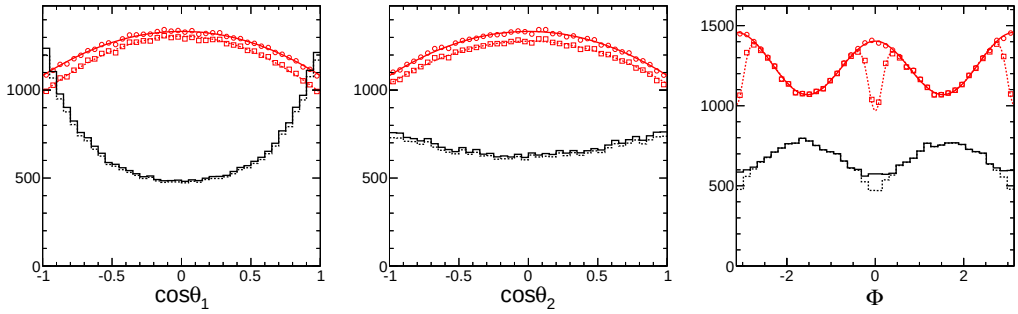

FIG. 23: Distributions of the observables in the $e^+e^- \to ZH$ analysis at $\sqrt{s} = 250$ GeV, from left to right: $\cos\theta_1$, $\cos\theta_2$, and Φ. Points (red) show simulated events for the SM Higgs boson with curves showing projections of analytical distributions. Histograms (black) show background distributions. Distributions before (solid) and after (dashed) detector acceptance effects are shown.

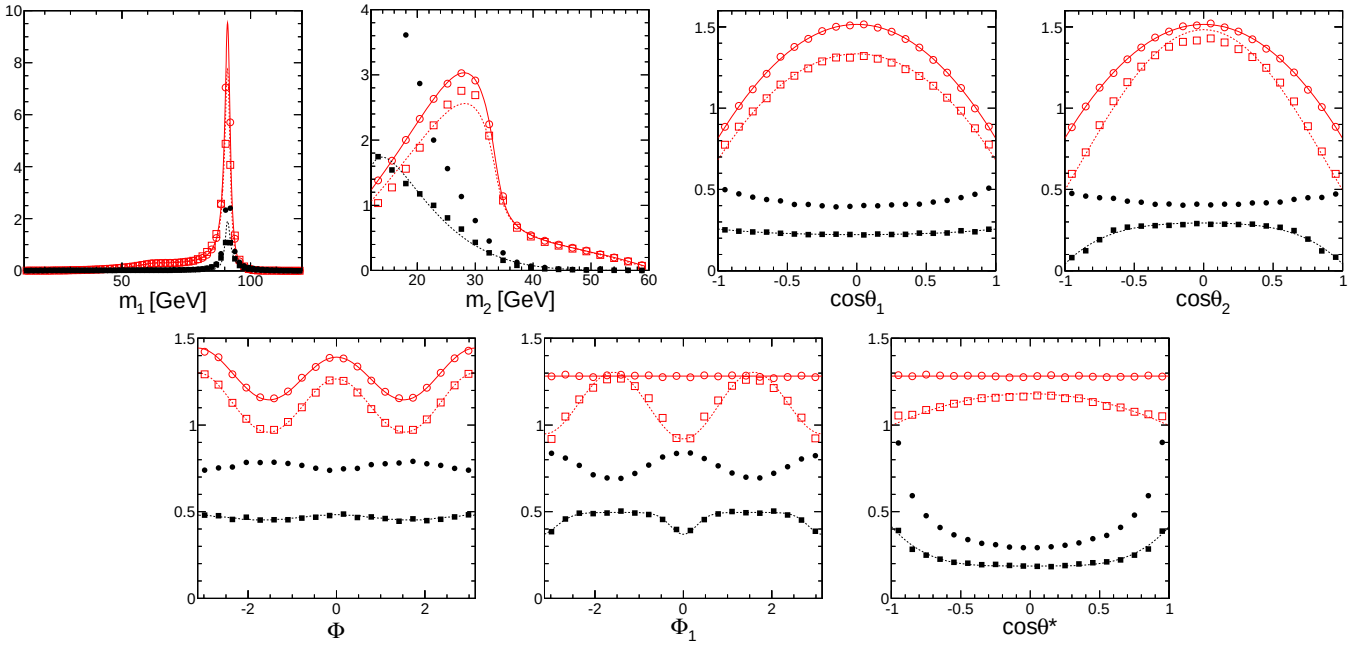

FIG. 24: Distributions of various observables (m_1, m_2, $\cos\theta_1$, $\cos\theta_2$, Φ, Φ_1, and $\cos\theta^*$) in the $H \to ZZ^* \to 4\ell$ analysis at the LHC. Open red points show simulated events for the SM Higgs boson with curves showing projections of analytical distributions. Solid black points show background distributions with curves showing projections of analytical parameterization. Distributions before (circles) and after (squares) detector acceptance effects are shown.

by the non-uniform function. We illustrate the effect on observables in the $e^+e^- \to ZH \to \ell\ell H$ analysis at $\sqrt{s} = 250$ GeV in Fig. 23, where the acceptance function from Eq. (B6) is implemented analytically.

Parameterization of background distributions, $\mathcal{P}_{\rm bkg}$, with multiple observables is also possible analytically. For example, in the $H \to ZZ^* \to 4f$ analysis, parameterization of the $q\bar{q} \to ZZ^*/Z\gamma^*$ process is available in Ref. [31], and detector effects can be included in a manner similar to what we described for the signal. Alternatively, a multi-dimensional template histogram can be used in place of such parameterization, potentially with proper smoothing of the distributions if there are sufficient statistics of simulated events. We have investigated both of these approaches for signal and background parameterization and found both of them feasible. However, some of the technical limitations include normalization of probabilities in multidimensional space, which may slow down the data analysis considerably. Therefore, for multi-parameter fits presented in this paper, we employ a simplified approach when both acceptance functions, $\mathcal{G}$, and background distributions, $\mathcal{P}_{\rm bkg}$, are approximated with analytical functions describing generated distributions in either one or two dimensions, see for example Fig. 24. The results of such studies are verified to give correct expectations for measurement precision by comparing to the expectations without detector effects or background (optimistic), and with the full treatment of detector effects and background using discriminant approach

as in Eq. (B3), which serve as two bounds of expected performance. In most cases, all three results provide similar expectations and we quote results from the multi-parameter fit. When analytical parameterization is not readily available, we quote results from the discriminant approach.

So far we have discussed the case of spin-zero boson, but the tools and ideas presented in this paper can be extended to any spin-parity study, such as multi-parameter fits of a spin-two hypothesis. In such a case, non-trivial $\cos\theta^*$ and Φ_1 distributions appear and depend on the production mechanism. It is desirable to extend the matrix element approach in such a way that it does not depend on the production model of a particle with non-zero spin but considers only its decay. This feature can be easily achieved by considering the unpolarized X-boson production by either averaging over the spin degrees of freedom of the produced X-boson or, equivalently, integrating over the two production angles $\cos\theta^*$ and Φ_1, defined in Fig. 1, in the probability distribution $\mathcal{P}$ [7, 8]. This leads to the following expression for the spin-averaged matrix element squared for the decay of a new boson X

$$\int \mathrm{d}\Phi_1 \mathrm{d}\cos\theta^* \; \mathcal{P}(m_1, m_2, \vec{\Omega}) \,. \tag{B7}$$

This method applies to any possible hypothesis with non-zero spin and small residual effects arising from detector acceptance can be addressed in experimental analysis. We provide tools that allow one to pursue this approach using both analytic and numerical computations of the probability distribution $\mathcal{P}$ [37].

[1] ATLAS collaboration, Phys. Lett. B **716**, 1 (2012).
[2] CMS collaboration, Phys. Lett. B **716**, 30 (2012).
[3] T. Aaltonen *et al.* (CDF collaboration, D0 collaboration), Phys. Rev. Lett. **109**, 071804 (2012).
[4] L. D. Landau, Dokl. Akad. Nauk SSSR **60**, 207 (1948); C. N. Yang, Phys. Rev. **77**, 242 (1950).
[5] CMS collaboration, S. Chatrchyan *et al.*, Phys. Rev. Lett. **110**, 081803 (2013), [arXiv:1212.6639 [hep-ex]]; preprints CMS-PAS-HIG-12-041, CMS-PAS-HIG-13-001, CMS-PAS-HIG-13-002, CMS-PAS-HIG-13-003, CMS-PAS-HIG-13-005, CMS-PAS-HIG-13-012, CMS-PAS-HIG-13-016.
[6] ATLAS collaboration, G. Aad *et al.*, arXiv:1307.1427 [hep-ex]; arXiv:1307.1432 [hep-ex]; preprints ATL-CONF-2013-013, ATL-CONF-2013-029, ATL-CONF-2013-031.
[7] Y.Y. Gao *et al.*, Phys. Rev. D **81**, 075022 (2010).
[8] S. Bolognesi *et al.*, Phys. Rev. D **86**, 095031 (2012).
[9] E. Accomando, A. G. Akeroyd, E. Akhmetzyanova, J. Albert *et al.*, hep-ph/0608079.
[10] LHC Higgs Cross Section Working Group Collaboration, S. Heinemeyer *et al.*, arXiv:1307.1347 [hep-ph].
[11] V. D. Barger, K. -m. Cheung, A. Djouadi, B. A. Kniehl and P. M. Zerwas, Phys. Rev. D **49**, 79 (1994) [hep-ph/9306270].
[12] T. Han and J. Jiang, Phys.Rev. **D** 63 (2001) 096007.
[13] T. Plehn *et al.*, Phys. Rev. Lett. **88** (2002) 051801.
[14] S.Y. Choi *et al.*, Phys.Lett. **B** 553 (2003), 61; Godbole, R. M., D. Miller, and M. M. Muhlleitner, JHEP 0712 (2007), 031.
[15] V. Hankele *et al.*, Phys.Rev. **D**74 (2006) 095001.
[16] V. Del Duca, G. Klamke, D. Zeppenfeld, M. L. Mangano, M. Moretti, F. Piccinini, R. Pittau and A. D. Polosa, JHEP **0610**, 016 (2006) [hep-ph/0608158].
[17] G. Mahlon and S. J. Parke, Phys. Rev. D **74**, 073001 (2006) [hep-ph/0606052].
[18] S. Dutta, K. Hagiwara, and Y. Matsumoto, Phys. Rev. **D**78 (2008) 115016.
[19] K. Hagiwara, Q. Li and K. Mawatari, JHEP **0907**, 101 (2009) [arXiv:0905.4314 [hep-ph]].
[20] S. D. Rindani and P. Sharma, Phys.Rev. **D** 79 (2009), 075007.
[21] S.S. Biswal *et al.*, Phys.Rev. **D**79 (2009), 035012.
[22] S. S. Biswal and R. M. Godbole, Phys.Lett. **B**680 (2009) 81.
[23] De Rujula, A. *et al*, Phys.Rev. D**82** (2010) 013003.
[24] N. D. Christensen *et al.*, Phys.Lett. **B**693 (2010) 28.
[25] N. Desai *et al.*, Phys.Rev. D83 (2011) 113004.
[26] J. S. Gainer, W. -Y. Keung, I. Low and P. Schwaller, Phys. Rev. D **86**, 033010 (2012) [arXiv:1112.1405 [hep-ph]].
[27] D. Stolarski *et al.*, Phys.Rev. D**86** (2012) 117504.
[28] J. Ellis *et al.*, JHEP 1211 (2012) 134.
[29] C. Englert *et al.*, JHEP 1206 (2012) 108.
[30] R. Boughezal, T. J. LeCompte and F. Petriello, arXiv:1208.4311 [hep-ph].
[31] Y. Chen, N. Tran and R. Vega-Morales, JHEP **1301**, 182 (2013) [arXiv:1211.1959 [hep-ph]]; J. S. Gainer, K. Kumar, I. Low and R. Vega-Morales, JHEP **1111**, 027 (2011) [arXiv:1108.2274 [hep-ph]].
[32] P. Artoisenet, P. de Aquino, F. Demartin, R. Frederix, S. Frixione, F. Maltoni, M. K. Mandal and P. Mathews *et al.*, arXiv:1306.6464 [hep-ph].
[33] C. Englert *et al.*, JHEP 1301 (2013) 148, [arXiv:1212.0843 [hep-ph]].
[34] A. Djouadi *et al.*, Phys. Lett. **B**723 (2013) 307.

[35] J. S. Gainer, J. Lykken, K. T. Matchev, S. Mrenna and M. Park, Phys. Rev. Lett. **111**, 041801 (2013) [arXiv:1304.4936 [hep-ph]].
[36] Y. Sun, X. -F. Wang and D. -N. Gao, arXiv:1309.4171 [hep-ph].
[37] The Monte-Carlo generator, the manual, and supporting material can be downloaded from http://www.pha.jhu.edu/spin/
[38] J. Alwall *et al.*, Comput. Phys. Commun. **176** (2007) 300.
[39] P. Nason, JHEP 0411 (2004) 040; S. Frixione, P. Nason, and C. Oleari, JHEP 0711 (2007) 070; S. Alioli, P. Nason, C. Oleari, and E. Re, JHEP 1006 (2010) 043.
[40] J. Alwall, M. Herquet, F. Maltoni, O. Mattelaer and T. Stelzer, JHEP **1106**, 128 (2011) [arXiv:1106.0522 [hep-ph]].
[41] K. Arnold, M. Bahr, G. Bozzi, F. Campanario, C. Englert, T. Figy, N. Greiner and C. Hackstein *et al.*, Comput. Phys. Commun. **180**, 1661 (2009) [arXiv:0811.4559 [hep-ph]].
[42] K. Arnold, J. Bellm, G. Bozzi, M. Brieg, F. Campanario, C. Englert, B. Feigl and J. Frank *et al.*, arXiv:1107.4038 [hep-ph].
[43] K. Arnold, J. Bellm, G. Bozzi, F. Campanario, C. Englert, B. Feigl, J. Frank and T. Figy *et al.*, arXiv:1207.4975 [hep-ph].
[44] T. Sjöstrand *et al.*, Comput. Phys. Commun. 178 (2008), 852.
[45] ATLAS Collaboration, arXiv:1307.7292 [hep-ex].
[46] CMS Collaboration, arXiv:1307.7135 [hep-ex].
[47] T. Behnke, J. E. Brau, B. Foster, J. Fuster, M. Harrison, J. M. Paterson, M. Peskin and M. Stanitzki *et al.*, arXiv:1306.6327 [physics.acc-ph].
[48] M. Koratzinos, A. P. Blondel, R. Aleksan, O. Brunner, A. Butterworth, P. Janot, E. Jensen and J. Osborne *et al.*, arXiv:1305.6498 [physics.acc-ph].
[49] J. M. Butterworth, A. R. Davison, M. Rubin and G. P. Salam, Phys. Rev. Lett. **100**, 242001 (2008) [arXiv:0802.2470 [hep-ph]].
[50] J. Shu and Y. Zhang, arXiv:1304.0773 [hep-ph].
[51] B. Grzadkowski and J. F. Gunion, Phys. Lett. B **294**, 361 (1992) [hep-ph/9206262].
[52] Particle Data Group, J. Beringer *et al.*, Phys. Rev. D **86**, 010001 (2012).
[53] J. M. Campbell, R. K. Ellis and C. Williams, JHEP **1107**, 018 (2011) [arXiv:1105.0020 [hep-ph]].
[54] N. Kauer and G. Passarino, JHEP **1208**, 116 (2012) [arXiv:1206.4803 [hep-ph]].
[55] F. Caola and K. Melnikov, arXiv:1307.4935 [hep-ph].
[56] P. Avery *et al.*, Phys. Rev. D **87**, 055006 (2013) [arXiv:1210.0896 [hep-ph]].
[57] J. Pumplin *et al.*, JHEP **0207**, 012 (2002).
[58] P. M. Nadolsky *et al.*, Phys. Rev. D **78**, 013004 (2008).
[59] N. Tran, Ph. D. thesis, Johns Hopkins University, CERN-THESIS-2011-127 (2011).
[60] CMS Collaboration, S. Chatrchyan *et al.*, Phys. Rev. D **84**, 112002 (2011) [arXiv:1110.2682 [hep-ex]].